Available online at www.sciencedirect.com
SCIENCE DIRECT®
Comput. Methods Appl. Mech. Engrg. 192 (2003) 1463–1494
Computer methods in applied mechanics and engineering
www.elsevier.com/locate/cma

T-stress, mixed-mode stress intensity factors, and crack initiation angles in functionally graded materials: a unified approach using the interaction integral method

Jeong-Ho Kim, Glaucio H. Paulino *

Department of Civil and Environmental Engineering, 2209 Newmark Laboratory, University of Illinois at Urbana-Champaign, 205 North Mathews Avenue, Urbana, IL 61801-2352, USA

Received 13 May 2002; received in revised form 11 December 2002

Abstract

For linear elastic functionally graded materials (FGMs), the fracture parameters describing the crack tip fields include not only stress intensity factors (SIFs) but also T-stress (nonsingular stress). These two fracture parameters are important for determining the crack initiation angle under mixed-mode loading conditions in brittle FGMs (e.g. ceramic/ceramic such as TiC/SiC). In this paper, the mixed-mode SIFs and T-stress are evaluated by means of the interaction integral, in the form of an equivalent domain integral, in combination with the finite element method. In order to predict the crack initiation angle in brittle FGMs, this paper makes use of a fracture criterion which incorporates the T-stress effect. This type of criterion involves the mixed-mode SIFs, the T-stress, and a physical length scale r_c (representative of the fracture process zone size). Various types of material gradations are considered such as continuum models (e.g. exponentially graded material) and micromechanics models (e.g. self-consistent model). Several examples are given to show the accuracy and efficiency of the interaction integral scheme for evaluating mixed-mode SIFs, T-stress, and crack initiation angle. The techniques developed provide a basic framework for quasi-static crack propagation in FGMs.

Keywords: Functionally graded material; T-stress; Stress intensity factor; Interaction integral; Finite element method

1. Introduction

Crack growth direction is important for assessing and enhancing structural integrity. Among several fracture criteria [1–3] developed to predict crack initiation angle, Erdogan and Sih [1] proposed the maximum hoop stress criterion, which has been successfully used for brittle materials. Williams and Ewing [4], and Ueda et al. [5] performed experiments using polymethyl-methacrylate (PMMA) with a slanted internal

* Corresponding author. Tel.: +1-217-333-3817; fax: +1-217-265-8041.
E-mail address: paulino@uiuc.edu (G.H. Paulino).

0045-7825/03/$ - see front matter © 2002 Elsevier Science B.V. All rights reserved.
doi:10.1016/S0045-7825(02)00652-7

crack, and found that there was a difference in crack initiation angles obtained by the maximum hoop stress criterion and by their experiments. They observed that the elastic T-stress, which is the nonsingular term in Williams [6] series expansion of stresses, has a significant influence on crack initiation angle. Thus to account for the difference, they modified the maximum hoop stress criterion into a generalized maximum hoop stress criterion, which incorporates the T-stress effect. For linearly elastic brittle materials, this criterion involves the mixed-mode stress intensity factors (SIFs), the T-stress, and the fracture process zone size r_c, which is assumed to be very small relative to the crack size and specimen dimensions. For instance, Chao and Zhang [7] adopted a set of experimental data obtained by Richardson and Goree [8], who experimented half-dogbone tension (HDT), compact tension (CT), single edge-notched tension (SENT), and delta tension (DT) specimens fabricated by using PMMA (Young's modulus $E = 2.76$ GPa, Yield stress $\sigma_Y = 55.2$ MPa, Toughness $K_c = 1.02$ MPa$\sqrt{\text{m}}$, Poisson's ratio $\nu = 0.33$). Based on curve fitting of PMMA tests, Chao and Zhang [7] found that $r_c \approx 0.5$ mm for stress-controlled fracture and $r_c \approx 0.03$ mm for strain-controlled fracture (the choice of the model depends on the fracture mechanisms of the material). Notice that both values are bigger than the plastic zone size estimated for brittle materials under plane strain, i.e. $r_p = (K_c/\sigma_Y)^2/8\pi \approx 0.0187$ mm, which somehow justifies the application of linear elastic crack tip fields. Moreover, based on experiments using thin plates of PMMA with an internal crack of length $2a$, Williams and Ewing [4] have suggested the critical parameter $c = \sqrt{2r_c/a} \approx 0.1$. This parameter was also advocated by Ueda et al. [5], although the actual physical reason for this parameter has not been clarified yet.

In the present work, the generalized maximum hoop stress criterion is extended to the functionally graded material (FGM) case. A methodology is presented to evaluate mixed-mode SIFs and T-stress for FGMs, and these basic parameters are used to predict crack initiation angle. Thus the Williams [6] asymptotic expansion of the stress field around the crack tip shown in Fig. 1 takes the form

$$\sigma_{ij} = \frac{K_{\mathrm{I}}}{\sqrt{2\pi r}} f_{ij}^{\mathrm{I}}(\theta) + \frac{K_{\mathrm{II}}}{\sqrt{2\pi r}} f_{ij}^{\mathrm{II}}(\theta) + T\delta_{1i}\delta_{1j} + \mathrm{O}(r^{1/2}), \tag{1}$$

where σ_{ij} denotes the stress tensor, K_{I} and K_{II} are the modes I and II SIFs, respectively, T is the nonsingular elastic T-stress, and the angular functions $f_{ij}(\theta)$ can be found in several references, e.g. [9].

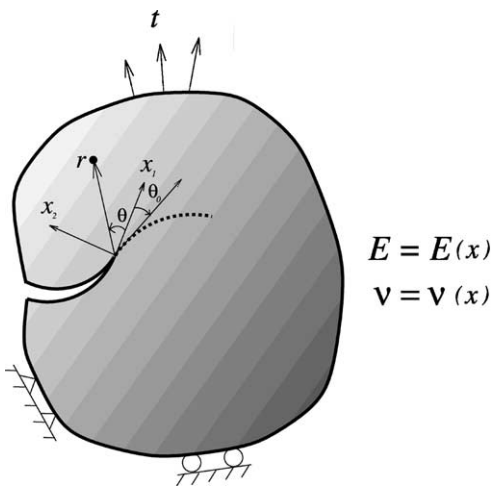

Fig. 1. Cartesian (x_1, x_2) and polar (r, θ) coordinates originating from the crack tip in an arbitrary FGM under traction (**t**) and displacement boundary conditions. The crack initiation angle is θ_0 (used subsequently).

Mixed-mode fracture of FGMs has been investigated primarily by evaluating mixed-mode SIFs of a stationary crack. Eischen [10] has evaluated mixed-mode SIFs in FGMs using the path-independent J_k^*-integral. Kim and Paulino [11] have also evaluated mixed-mode SIFs in FGMs by means of the path-independent J_k^*-integral using the equivalent domain integral (EDI). Marur and Tippur [12] have investigated a crack perpendicular to the material gradation by performing finite element analyses in conjunction with experiments. Yau et al. [13] proposed the interaction integral method for evaluating SIFs in homogeneous isotropic solids. The method is based on conservation laws of elasticity and fracture mechanics concepts. It makes use of a conservation integral for two admissible states of an elastic solid: actual and auxiliary states. Wang et al. [14] extended the method to homogeneous orthotropic solids. Yau [15] also used the method for bimaterial interface problems. Recently, the interaction integral method has emerged as an accurate and robust scheme for evaluating SIFs in FGMs [16–18]. For instance, Dolbow and Gosz [16] considered the plane problem of an arbitrarily oriented crack and used the extended finite element method (X-FEM), Rao and Rahman [17] used the element-free Galerkin (EFG) method, and Kim and Paulino [18] used the FEM to investigate FGMs with multiple cracks and material properties determined by means of either continuum functions (e.g. exponentially graded materials) or micromechanics models (e.g. self-consistent, Mori–Tanaka, or three-phase model). For the reasons described above, the interaction integral is the method of choice in this work.

Although SIFs are well-known fracture parameters, T-stress is less understood, and thus its implications in fracture of FGMs need to be investigated further. For homogeneous materials, T-stress has a significant influence on crack growth under mixed-mode loading [4,5,19] and crack path stability in mode I loading considering a small imperfection [20]. T-stress has been also shown to have a significant influence on crack-tip constraint and toughness [21,22]. Because of the importance of T-stress in fracture, investigations of T-stress have been extensively performed for homogeneous materials. Larsson and Carlsson [23] investigated T-stress in mode I loading and found that it affects the size and shape of the plastic zone. Leevers and Radon [24] used a variational formulation to evaluate T-stress. Afterwards, Cardew et al. [25] and Kfouri [26] used the path-independent J-integral in conjunction with the interaction integral to calculate T-stress in mode I crack problems. Sladek et al. [27] used another type of path-independent integral, based on Betti–Rayleigh reciprocal theorem, for evaluating T-stress in mixed-mode loading. Recently Chen et al. [28] investigated T-stress under mode I loading by means of both the Betti–Rayleigh reciprocal theorem and Eshelby's energy momentum tensor (i.e. path-independent J-integral) using the p-version finite element method, and addressed the accuracy of numerical computations.

For brittle FGMs (e.g. $MoSi_2$/SiC [29], TiC/SiC [30]), T-stress is also considered to have a significant influence in crack initiation angle and crack stability. However, it is worth mentioning that the present analysis is **not** analogous to the influence of T-stress in changing "constraint", as discussed in many references [21–23,31]. Considerations of "constraint" are **not** applicable to the analysis of ideal linearly elastic brittle materials (cf. [19]). Recent work in the field of FGMs include that by Becker et al. [32] who have investigated T-stress and finite crack kinking by using a hyperbolic-tangent material gradation with steep gradient of Young's modulus. They found that T-stress in FGMs is affected by both the far-field loading and the far-field phase angle, and that the magnitude of T-stress in FGMs is, on average, greater than that for homogeneous materials with identical geometry. They calculated T-stress using the stress difference along $\theta = 0$, i.e. $\sigma_{xx} - \sigma_{yy}$. On the other hand, Paulino and Kim [33] evaluated T-stress in FGMs using the interaction integral in conjunction with the FEM, and obtained quite accurate results.

In this paper, both mixed-mode SIFs and T-stress in brittle FGMs are evaluated through a unified approach, which makes use of the interaction integral method. This method is implemented for FGMs with general material properties including either continuum functions or micromechanics models (e.g. self-consistent, differential or Mori–Tanaka method (MT)). Sometimes the effects of a material being functionally graded rather than homogeneous turn out be minor, but sometimes they are dramatic, as illustrated in this work.

This paper is organized as follows. Section 2 presents auxiliary fields chosen for SIFs and T-stress in the interaction integral (M-integral) method. Section 3 explains the M-integral formulation for FGMs together with its underlying solution procedures and numerical aspects. Section 4 establishes the relationships between M-integral and SIFs. Section 5 presents the extraction of the T-stress from the M-integral. Section 6 outlines selected micromechanics models used for the analysis. Section 7 explains the generalized maximum hoop stress criterion, which includes the T-stress effect. Section 8 presents various features of the finite element implementation. Section 9 presents various examples. Finally, Section 10 provides some conclusions and potential extensions of this work.

2. Auxiliary fields

The interaction integral makes use of the auxiliary fields, such as stresses ($\boldsymbol{\sigma}^{\text{aux}}$), strains ($\boldsymbol{\varepsilon}^{\text{aux}}$) and displacements ($\boldsymbol{u}^{\text{aux}}$). These auxiliary fields have to be suitably defined in order to evaluate mixed-mode SIFs and T-stress. There are various choices for the auxiliary fields. Here we adopt fields originally developed for homogeneous materials and use an ''incompatible formulation'' which accounts for the displacement mismatch between the homogeneous and graded materials. The auxiliary fields chosen in this paper are described below.

2.1. Auxiliary fields for SIFs

For evaluating mixed-mode SIFs, we select the auxiliary stress and displacement fields as the Williams' [6] crack-tip asymptotic fields (i.e. $\mathrm{O}(r^{-1/2})$ for the stress field and $\mathrm{O}(r^{1/2})$ for the displacement field) with the material properties sampled at the crack-tip location [10,34]. Fig. 1 shows a crack in an FGM under two-dimensional (2D) fields in local Cartesian and polar coordinates originating at the crack tip. The auxiliary stress and displacement fields are chosen as:

$$\sigma_{ij}^{\text{aux}} = \frac{K_{\text{I}}^{\text{aux}}}{\sqrt{2\pi r}} f_{ij}^{\text{I}}(\theta) + \frac{K_{\text{II}}^{\text{aux}}}{\sqrt{2\pi r}} f_{ij}^{\text{II}}(\theta), \tag{2}$$

$$u_i^{\text{aux}} = \frac{K_{\text{I}}^{\text{aux}}}{\mu_{\text{tip}}} \sqrt{\frac{r}{2\pi}} g_i^{\text{I}}(\theta) + \frac{K_{\text{II}}^{\text{aux}}}{\mu_{\text{tip}}} \sqrt{\frac{r}{2\pi}} g_i^{\text{II}}(\theta), \ \ (i,j=1,2) \tag{3}$$

respectively, where μ_{tip} is the shear modulus at the crack tip, and $K_{\text{I}}^{\text{aux}}$ and $K_{\text{II}}^{\text{aux}}$ are the auxiliary modes I and II SIFs, respectively, and the angular functions $f_{ij}(\theta)$ and $g_i(\theta)$ are given in several references, e.g. [9].

2.2. Auxiliary fields for T-stress

For evaluating T-stress, we choose the auxiliary stress and displacement fields as those due to a point force in the x_1 direction, applied to the tip of a semi-infinite crack in an infinite homogeneous body as shown in Fig. 2. The auxiliary stresses are given by [35]:

$$\sigma_{11}^{\text{aux}} = -\frac{f}{\pi r}\cos^3\theta, \quad \sigma_{22}^{\text{aux}} = -\frac{f}{\pi r}\cos\theta\sin^2\theta, \quad \sigma_{12}^{\text{aux}} = -\frac{f}{\pi r}\cos^2\theta\sin\theta. \tag{4}$$

The corresponding auxiliary displacements are [35]:

$$u_1^{\text{aux}} = -\frac{f(1+\kappa_{\text{tip}})}{8\pi\mu_{\text{tip}}}\ln\frac{r}{d} - \frac{f}{4\pi\mu_{\text{tip}}}\sin^2\theta,$$

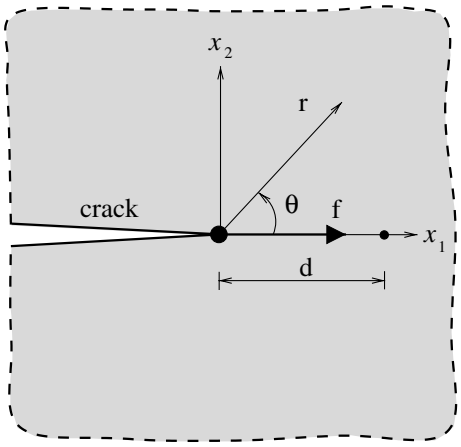

Fig. 2. A point force applied at the crack tip in the direction parallel to the crack in an infinite homogeneous medium.

$$u_2^{\text{aux}} = -\frac{f(\kappa_{\text{tip}} - 1)}{8\pi\mu_{\text{tip}}}\theta + \frac{f}{4\pi\mu_{\text{tip}}}\sin\theta\cos\theta, \tag{5}$$

where d is the coordinate of a fixed point on the x_1 axis (see Fig. 2), μ_{tip} is the shear modulus at the crack tip, and κ_{tip} is $(3 - \nu_{\text{tip}})/(1 + \nu_{\text{tip}})$ for generalized plane stress and $(3 - 4\nu_{\text{tip}})$ for plane strain.

2.3. Auxiliary strains—incompatible formulation

Notice that the auxiliary stress fields in Eqs. (2) and (4) are in equilibrium, i.e. $\sigma_{ij,j}^{\text{aux}} = 0$ (no body forces or inertia). However, the auxiliary strain field is chosen as

$$\varepsilon_{ij}^{\text{aux}} = S_{ijkl}(\boldsymbol{x})\sigma_{kl}^{\text{aux}}, \tag{6}$$

which differs from

$$\varepsilon_{ij}^{\text{aux}} = (S_{ijkl})_{\text{tip}}\sigma_{kl}^{\text{aux}}, \tag{7}$$

where $S_{ijkl}(\boldsymbol{x})$ is the compliance tensor of the actual FGM and $(S_{ijkl})_{\text{tip}}$ is the compliance tensor at the crack tip. Thus, the auxiliary strain field in Eq. (6) is incompatible with the auxiliary displacement fields in Eqs. (3) and (5) i.e. $\varepsilon_{ij}^{\text{aux}} \neq (u_{i,j}^{\text{aux}} + u_{j,i}^{\text{aux}})/2$, where $\varepsilon_{ij}^{\text{aux}}$ is given by Eq. (6). This incompatibility in the strain field has to be taken into account in the interaction integral formulation, which is discussed in detail below.

3. A unified approach for SIFs and T-stress evaluation

The interaction integral is obtained as a cross-term in superimposed states of the path-independent J-integral [36], which involves two admissible configurations of a cracked elastic FGM body. The present formulation of the interaction integral is valid for both SIFs and T-stress. In the theoretical part of the derivation, the path-independent J-integral is converted into an EDI [37] using a (numerical) weight function q. Moreover, for implementation purposes, the interaction integral is evaluated in terms of the global coordinates and then transferred to the local coordinates.

3.1. Interaction integral: formulation

The J-integral [36] is defined as

$$J = \lim_{\Gamma_s \to 0} \int_{\Gamma_s} (\mathscr{W}\delta_{1j} - \sigma_{ij}u_{i,1})n_j \, \mathrm{d}\Gamma, \tag{8}$$

where $\mathscr{W}$ is the strain energy density given by

$$\mathscr{W} = \tfrac{1}{2}\sigma_{ij}\varepsilon_{ij} = \tfrac{1}{2}C_{ijkl}\varepsilon_{kl}\varepsilon_{ij}, \tag{9}$$

and n_j is the outward normal vector to the contour Γ_s, as shown in Fig. 3. To convert the contour integral into an EDI, one defines the following contour integral:

$$\mathscr{H} = \oint_{\Gamma} (W\delta_{1j} - \sigma_{ij}u_{i,1})m_j q \, \mathrm{d}\Gamma, \tag{10}$$

where $\Gamma = \Gamma_0 + \Gamma^+ - \Gamma_s + \Gamma^-$, m_j is a unit vector outward normal to the corresponding contour (i.e. $m_j = n_j$ on Γ_0 and $m_j = -n_j$ on Γ_s), and q is a weight function defined as a smoothly varying function from $q = 1$ on Γ_s to $q = 0$ on Γ_0 (see Fig. 4). Taking the limit $\Gamma_s \to 0$ leads to

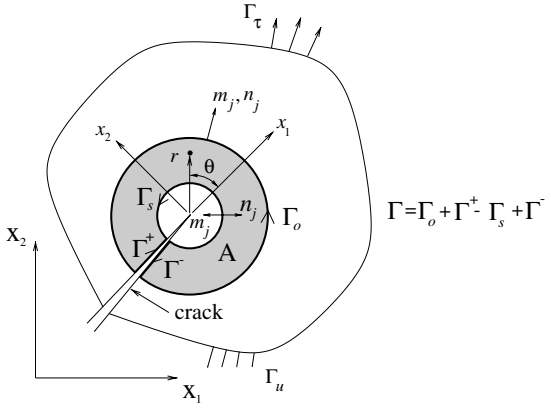

Fig. 3. Conversion of the contour integral into an EDI. Here $\Gamma = \Gamma_0 + \Gamma^+ - \Gamma_s + \Gamma^-$, $m_j = n_j$ on Γ_0 and $m_j = -n_j$ on Γ_s.

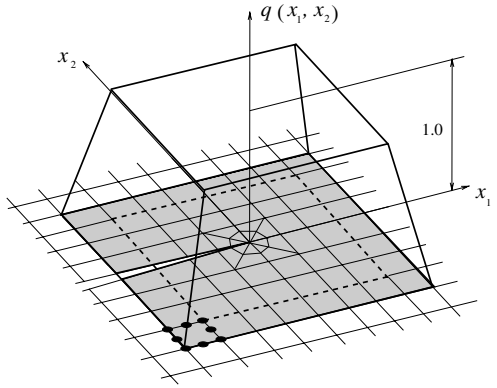

Fig. 4. Plateau weight function (q function).

$$\begin{aligned}\lim_{\Gamma_s\to 0}\mathscr{H} &= \lim_{\Gamma_s\to 0}\oint_{\Gamma}(\mathscr{W}\delta_{1j}-\sigma_{ij}u_{i,1})m_j q\,\mathrm{d}\Gamma\\ &= \lim_{\Gamma_s\to 0}\int_{\Gamma_0+\Gamma^+\Gamma^--\Gamma_s}(\mathscr{W}\delta_{1j}-\sigma_{ij}u_{i,1})m_j q\,\mathrm{d}\Gamma\\ &= \lim_{\Gamma_s\to 0}\left[\int_{\Gamma_0+\Gamma^+\Gamma^-}(\mathscr{W}\delta_{1j}-\sigma_{ij}u_{i,1})m_j q\,\mathrm{d}\Gamma+\int_{-\Gamma_s}(\mathscr{W}\delta_{1j}-\sigma_{ij}u_{i,1})m_j q\,\mathrm{d}\Gamma\right]\\ &= \lim_{\Gamma_s\to 0}\left[\int_{\Gamma_0+\Gamma^+\Gamma^-}(\mathscr{W}\delta_{1j}-\sigma_{ij}u_{i,1})m_j q\,\mathrm{d}\Gamma-\int_{\Gamma_s}(\mathscr{W}\delta_{1j}-\sigma_{ij}u_{i,1})n_j q\,\mathrm{d}\Gamma\right].\end{aligned}\tag{11}$$

Because $q=0$ on Γ_0 and the crack faces are assumed to be traction-free, Eq. (11) becomes

$$J=-\lim_{\Gamma_s\to 0}\mathscr{H}=-\lim_{\Gamma_s\to 0}\oint_{\Gamma}(\mathscr{W}\delta_{1j}-\sigma_{ij}u_{i,1})m_j q\,\mathrm{d}\Gamma.\tag{12}$$

Now applying the divergence theorem to Eq. (12), one obtains the following EDI

$$J=\int_A(\sigma_{ij}u_{i,1}-\mathscr{W}\delta_{1j})q_{,j}\,\mathrm{d}A+\int_A(\sigma_{ij}u_{i,1}-\mathscr{W}\delta_{1j})_{,j}q\,\mathrm{d}A.\tag{13}$$

Using Eq. (9) and the derivative of strain energy density given as

$$\mathscr{W}_{,1}=\frac{\partial\mathscr{W}}{\partial x_1}=\sigma_{ij}\varepsilon_{ij,1}+\frac{1}{2}C_{ijkl,1}\varepsilon_{kl}\varepsilon_{ij},\tag{14}$$

where $C_{ijkl}=C_{ijkl}(\boldsymbol{x})$ is the constitutive tensor of FGMs, one obtains

$$J=\int_A(\sigma_{ij}u_{i,1}-\mathscr{W}\delta_{1j})q_{,j}\,\mathrm{d}A+\int_A\left\{\underline{\sigma_{ij}(u_{i,1j}-\varepsilon_{ij,1})}-\frac{1}{2}C_{ijkl,1}\varepsilon_{kl}\varepsilon_{ij}\right\}q\,\mathrm{d}A.\tag{15}$$

Notice that the underlined terms in Eq. (15) must vanish for the actual fields, but we retain them for the purpose of extracting the ''incompatible'' terms, which will arise in the interaction integral. For two admissible fields which are the actual $(\boldsymbol{u},\boldsymbol{\varepsilon},\boldsymbol{\sigma})$ and auxiliary $(\boldsymbol{u}^{\mathrm{aux}},\boldsymbol{\varepsilon}^{\mathrm{aux}},\boldsymbol{\sigma}^{\mathrm{aux}})$ fields, the superimposed J-integral, J^s, is given by

$$J^s=J+J^{\mathrm{aux}}+M,\tag{16}$$

where J is given by Eq. (15), J^{aux} is given by

$$J^{\mathrm{aux}}=\int_A(\sigma_{ij}^{\mathrm{aux}}u_{i,1}^{\mathrm{aux}}-\mathscr{W}^{\mathrm{aux}}\delta_{1j})q_{,j}\,\mathrm{d}A+\int_A\left\{\sigma_{ij}^{\mathrm{aux}}(u_{i,1j}^{\mathrm{aux}}-\varepsilon_{ij,1}^{\mathrm{aux}})-\frac{1}{2}C_{ijkl,1}\varepsilon_{kl}^{\mathrm{aux}}\varepsilon_{ij}^{\mathrm{aux}}\right\}q\,\mathrm{d}A\tag{17}$$

and M is the so-called interaction integral, which is given by

$$\begin{aligned}M=&\int_A\left\{(\sigma_{ij}u_{i,1}^{\mathrm{aux}}+\sigma_{ij}^{\mathrm{aux}}u_{i,1})-\frac{1}{2}(\sigma_{ik}\varepsilon_{ik}^{\mathrm{aux}}+\sigma_{ik}^{\mathrm{aux}}\varepsilon_{ik})\delta_{1j}\right\}q_{,j}\,\mathrm{d}A\\&+\int_A\left\{\sigma_{ij}(u_{i,1j}^{\mathrm{aux}}-\varepsilon_{ij,1}^{\mathrm{aux}})+\sigma_{ij}^{\mathrm{aux}}(u_{i,1j}-\varepsilon_{ij,1})-\frac{1}{2}C_{ijkl,1}(\varepsilon_{ij}\varepsilon_{kl}^{\mathrm{aux}}+\varepsilon_{ij}^{\mathrm{aux}}\varepsilon_{kl})\right\}q\,\mathrm{d}A.\end{aligned}\tag{18}$$

After algebraic manipulations involving the following equalities

$$\sigma_{ij}^{\mathrm{aux}}u_{i,1j}=\sigma_{ij}^{\mathrm{aux}}\varepsilon_{ij,1},\quad \sigma_{ij}\varepsilon_{ij}^{\mathrm{aux}}=\sigma_{ij}^{\mathrm{aux}}\varepsilon_{ij},\quad C_{ijkl,1}\varepsilon_{ij}^{\mathrm{aux}}\varepsilon_{kl}=C_{ijkl,1}\varepsilon_{ij}\varepsilon_{kl}^{\mathrm{aux}},\tag{19}$$

one obtains

$$M = (M_1)_{\text{local}} = \int_A \left\{ (\sigma_{ij} u^{\text{aux}}_{i,1} + \sigma^{\text{aux}}_{ij} u_{i,1}) - \frac{1}{2}(\sigma_{ik}\varepsilon^{\text{aux}}_{ik} + \sigma^{\text{aux}}_{ik}\varepsilon_{ik})\delta_{1j} \right\} q_{,j}\, \mathrm{d}A + \int_A \left\{ \underline{\sigma_{ij}(u^{\text{aux}}_{i,1j} - \varepsilon^{\text{aux}}_{ij,1})} - C_{ijkl,1}\varepsilon_{ij}\varepsilon^{\text{aux}}_{kl} \right\} q\, \mathrm{d}A. \tag{20}$$

Notice that the incompatibility terms, underlined in Eq. (20), arise naturally in the M-integral formulation for FGMs.

3.2. Interaction integral: numerical aspects

For numerical computation by means of the FEM, the M-integral is evaluated first in the global coordinates (M_{global}) and then transformed to the local coordinates (M_{local}). The global interaction integral $(M_m)_{\text{global}}$ is obtained as ($m = 1, 2$)

$$(M_m)_{\text{global}} = \int_A \left\{ (\sigma_{ij} u^{\text{aux}}_{i,m} + \sigma^{\text{aux}}_{ij} u_{i,m}) - \frac{1}{2}(\sigma_{ik}\varepsilon^{\text{aux}}_{ik} + \sigma^{\text{aux}}_{ik}\varepsilon_{ik})\delta_{mj} \right\} \frac{\partial q}{\partial X_j}\, \mathrm{d}A + \int_A \left\{ \underline{\sigma_{ij}(u^{\text{aux}}_{i,mj} - \varepsilon^{\text{aux}}_{ij,m})} - C_{ijkl,m}\varepsilon_{ij}\varepsilon^{\text{aux}}_{kl} \right\} q\, \mathrm{d}A, \tag{21}$$

where (X_1, X_2) are the global coordinates shown in Fig. 3 and the derivatives of the auxiliary strain fields $\varepsilon^{\text{aux}}_{ij,m}$ must be carefully evaluated according to the details explained by Kim and Paulino [18]. The following transformation ($i, j = 1, 2$)

$$(M_i)_{\text{local}} = \alpha_{ij}(\theta)(M_i)_{\text{global}}, \alpha_{ij}(\theta) = \begin{bmatrix} \cos\theta & \sin\theta \\ -\sin\theta & \cos\theta \end{bmatrix}, \tag{22}$$

allows one to calculate M_{local} as

$$M_{\text{local}} = (M_1)_{\text{local}} = (M_1)_{\text{global}} \cos\theta + (M_2)_{\text{global}} \sin\theta. \tag{23}$$

For general material gradations, such as those obtained by means of micromechanics models, there are no closed-form expressions for derivatives of material properties. Thus special consideration should be taken for these derivatives, i.e. derivatives of the auxiliary strain field $\varepsilon^{\text{aux}}_{ij,m}$ and derivatives of the constitutive tensor $C_{ijkl,m}$ in Eq. (21). *For the sake of numerical efficiency, a general approach is used in all the examples, which includes exponentially graded materials, hyperbolic-tangent materials, and micromechanics-based materials.* The derivatives of the auxiliary strain field are obtained as:

$$\varepsilon^{\text{aux}}_{ij,m} = S_{ijkl,m}\sigma^{\text{aux}}_{kl} + S_{ijkl}\sigma^{\text{aux}}_{kl,m}. \tag{24}$$

A simple and accurate approach consists of evaluating $C_{ijkl,m}$ (see Eq. (21)) and $S_{ijkl,m}$ (see Eq. (24)) by using shape function derivatives. The derivatives of the material quantity P (e.g. C_{ijkl} and S_{ijkl}) are obtained as

$$\frac{\partial P}{\partial X_m} = \sum_{i=1}^{n} \frac{\partial N_i}{\partial X_m} P_i, \quad (m = 1, 2), \tag{25}$$

where n is the number of element nodes and $N_i = N_i(\xi, \eta)$ are the shape functions which can be found in many references, e.g. [38]. The derivatives $\partial N_i/\partial X_m$ are obtained as

$$\begin{Bmatrix} \partial N_i/\partial X_1 \\ \partial N_i/\partial X_2 \end{Bmatrix} = \boldsymbol{J}^{-1} \begin{Bmatrix} \partial N_i/\partial \xi \\ \partial N_i/\partial \eta \end{Bmatrix}, \tag{26}$$

where $\boldsymbol{J}^{-1}$ is the inverse of the standard Jacobian matrix given by

$$\boldsymbol{J} = \begin{bmatrix} \partial X_1/\partial\xi & \partial X_2/\partial\xi \\ \partial X_1/\partial\eta & \partial X_2/\partial\eta \end{bmatrix}. \tag{27}$$

4. Evaluation of SIFs

The relationship between J-integral and the modes I and II SIFs is given as:

$$J_{\text{local}} = \frac{K_{\text{I}}^2 + K_{\text{II}}^2}{E'_{\text{tip}}}, \tag{28}$$

where $E'_{\text{tip}} = E_{\text{tip}}$ for generalized plane stress and $E_{\text{tip}}/(1 - \nu_{\text{tip}}^2)$ for plane strain. For two admissible fields, which are the actual $(\boldsymbol{u}, \boldsymbol{\varepsilon}, \boldsymbol{\sigma})$ and auxiliary $(\boldsymbol{u}^{\text{aux}}, \boldsymbol{\varepsilon}^{\text{aux}}, \boldsymbol{\sigma}^{\text{aux}})$ fields, one obtains [13]

$$J^s_{\text{local}} = \frac{(K_{\text{I}} + K_{\text{I}}^{\text{aux}})^2 + (K_{\text{II}} + K_{\text{II}}^{\text{aux}})^2}{E'_{\text{tip}}}, \tag{29}$$

$$= J_{\text{local}} + J^{\text{aux}}_{\text{local}} + M_{\text{local}}, \tag{30}$$

where J_{local} is given by Eq. (28), $J^{\text{aux}}_{\text{local}}$ is given by

$$J^{\text{aux}}_{\text{local}} = \frac{(K_{\text{I}}^{\text{aux}})^2 + (K_{\text{II}}^{\text{aux}})^2}{E'_{\text{tip}}} \tag{31}$$

and M_{local} is given by

$$M_{\text{local}} = \frac{2}{E'_{\text{tip}}}(K_{\text{I}}K_{\text{I}}^{\text{aux}} + K_{\text{II}}K_{\text{II}}^{\text{aux}}). \tag{32}$$

The modes I and II SIFs are decoupled and are evaluated as follows:

$$K_{\text{I}} = \frac{E'_{\text{tip}}}{2} M_{\text{local}} \quad (K_{\text{I}}^{\text{aux}} = 1.0, K_{\text{II}}^{\text{aux}} = 0.0), \tag{33}$$

$$K_{\text{II}} = \frac{E'_{\text{tip}}}{2} M_{\text{local}} \quad (K_{\text{I}}^{\text{aux}} = 0.0, K_{\text{II}}^{\text{aux}} = 1.0). \tag{34}$$

The relationships of Eqs. (33) and (34) are the same as those for homogeneous materials [13] except that, for FGMs, the material properties are evaluated at the crack-tip location [16–18].

5. Evaluation of T-stress

The T-stress (nonsingular constant stress) can be extracted from the interaction integral by nullifying the contributions of both singular (i.e. $\text{O}(r^{-1/2})$) and higher-order (i.e. $\text{O}(r^{1/2})$ and higher) terms. The contribution of the singular terms will be discussed later, and the contribution of the higher-order terms is canceled by taking the limit $r \to 0$ of the domain A shown in Fig. 3. By doing so, the incompatibility terms of Eq. (20),

$$\int_A \underline{\sigma_{ij}(u^{\text{aux}}_{i,1j} - \varepsilon^{\text{aux}}_{ij,1})} q \, \mathrm{d}A, \tag{35}$$

naturally vanish because the auxiliary fields are compatible very near the crack tip (asymptotically), i.e. $\varepsilon_{ij}^{\text{aux}} = (u_{i,j}^{\text{aux}} + u_{j,i}^{\text{aux}})/2$ due to $\varepsilon_{ij}^{\text{aux}} = (S_{ijkl})_{\text{tip}}\sigma_{kl}^{\text{aux}}$. Furthermore, the second domain integral which includes $C_{ijkl,1}(\boldsymbol{x})$ in $(M_1)_{\text{local}}$ of Eq. (20),

$$\int_A C_{ijkl,1}\varepsilon_{ij}\varepsilon_{kl}^{\text{aux}} q \,\mathrm{d}A \tag{36}$$

also vanishes for the following reason. The derivatives of the elastic moduli $C_{ijkl,1}(\boldsymbol{x})$ are assumed to be bounded at the crack tip, i.e. $\mathrm{O}(r^{\alpha})$ with $\alpha \geqslant 0$. Therefore the second domain integral of Eq. (20) becomes

$$\begin{aligned}\lim_{r\to 0}\int_A C_{ijkl,1}\varepsilon_{ij}\varepsilon_{kl}^{\text{aux}} q \,\mathrm{d}A &= \lim_{r\to 0}\int_{-\pi}^{\pi}\int_0^r C_{ijkl,1}\varepsilon_{ij}\varepsilon_{kl}^{\text{aux}} q r \,\mathrm{d}r\,\mathrm{d}\theta \\ &= \lim_{r\to 0}\int_{-\pi}^{\pi}\int_0^r \mathrm{O}(r^{\alpha})\mathrm{O}(r^{-1/2})\mathrm{O}(r^{-1}) q r \,\mathrm{d}r\,\mathrm{d}\theta \\ &= \lim_{r\to 0}\mathrm{O}(r^{\alpha+1/2}) = 0.\end{aligned} \tag{37}$$

Then the interaction integral of Eq. (20) becomes

$$M_{\text{local}} = \int_A \left\{(\sigma_{ij}u_{i,1}^{\text{aux}} + \sigma_{ij}^{\text{aux}}u_{i,1}) - \frac{1}{2}(\sigma_{ik}\varepsilon_{ik}^{\text{aux}} + \sigma_{ik}^{\text{aux}}\varepsilon_{ik})\delta_{1j}\right\} q_{,j}\,\mathrm{d}A \tag{38}$$

which has the same form as the expression for homogeneous materials. Eq. (38) can be rewritten as

$$M_{\text{local}} = \int_A \left[\left\{(\sigma_{ij}u_{i,1}^{\text{aux}} + \sigma_{ij}^{\text{aux}}u_{i,1}) - \frac{1}{2}(\sigma_{ik}\varepsilon_{ik}^{\text{aux}} + \sigma_{ik}^{\text{aux}}\varepsilon_{ik})\delta_{1j}\right\} q\right]_{,j}\mathrm{d}A, \tag{39}$$

because its expansion leads to

$$\begin{aligned}M_{\text{local}} = &\int_A \left\{(\sigma_{ij}u_{i,1}^{\text{aux}} + \sigma_{ij}^{\text{aux}}u_{i,1}) - \frac{1}{2}(\sigma_{ik}\varepsilon_{ik}^{\text{aux}} + \sigma_{ik}^{\text{aux}}\varepsilon_{ik})\delta_{1j}\right\} q_{,j}\,\mathrm{d}A \\ &+ \int_A \left\{(\sigma_{ij}u_{i,1}^{\text{aux}} + \sigma_{ij}^{\text{aux}}u_{i,1}) - \frac{1}{2}(\sigma_{ik}\varepsilon_{ik}^{\text{aux}} + \sigma_{ik}^{\text{aux}}\varepsilon_{ik})\delta_{1j}\right\}_{,j} q\,\mathrm{d}A\end{aligned} \tag{40}$$

and the second domain integral of Eq. (40) vanishes after some algebraic manipulation. Now applying divergence theorem to convert the EDI of Eq. (39) into a line integral yields

$$M_{\text{local}} = \lim_{\Gamma_s\to 0}\oint_{\Gamma}\left\{(\sigma_{ij}u_{i,1}^{\text{aux}} + \sigma_{ij}^{\text{aux}}u_{i,1}) - \frac{1}{2}(\sigma_{ik}\varepsilon_{ik}^{\text{aux}} + \sigma_{ik}^{\text{aux}}\varepsilon_{ik})\delta_{1j}\right\} m_j q\,\mathrm{d}\Gamma. \tag{41}$$

Since $m_j = -n_j$ and $q = 1$ on Γ_s, $m_j = n_j$ and $q = 0$ on Γ_0, and the crack faces are assumed to be traction-free, Eq. (41) becomes

$$M_{\text{local}} = \lim_{\Gamma_s\to 0}\int_{\Gamma_s}\left[\frac{1}{2}(\sigma_{ik}\varepsilon_{ik}^{\text{aux}} + \sigma_{ik}^{\text{aux}}\varepsilon_{ik})\delta_{1j} - (\sigma_{ij}u_{i,1}^{\text{aux}} + \sigma_{ij}^{\text{aux}}u_{i,1})\right] n_j\,\mathrm{d}\Gamma. \tag{42}$$

Now let's check the contribution of the singular terms $\mathrm{O}(r^{-1/2})$ to the interaction integral. The actual stress field is given by Eq. (1), and the auxiliary stress field is given by Eq. (4). As the contour Γ_s shrinks to the crack tip region, the higher-order terms cancel out as mentioned above, and the only term that contributes to M_{local} is the term involving T. In other words, there is no contribution from the singular terms because the integration of sigmoidal functions (coefficients of the singular term $\mathrm{O}(r^{-1/2})$) with respect to $\theta = -\pi$ to $+\pi$ becomes zero regardless of the singularity of $\mathrm{O}(r^{-1/2})$. Therefore we can consider only the stress parallel to the crack direction:

$$\sigma_{ij} = T\delta_{1i}\delta_{1j}. \tag{43}$$

Using the stress–strain and strain–displacement relationships, one obtains

$$u_{1,1} = \varepsilon_{11} = \frac{1+\kappa(\boldsymbol{x})}{8\mu(\boldsymbol{x})}T, \quad u_{2,2} = \varepsilon_{22} = \frac{\kappa(\boldsymbol{x})-3}{8\mu(\boldsymbol{x})}T, \quad u_{1,2}+u_{2,1} = 0, \tag{44}$$

for the actual fields; and

$$u^{\text{aux}}_{1,1} = \varepsilon^{\text{aux}}_{11} = \frac{1+\kappa(\boldsymbol{x})}{8\mu(\boldsymbol{x})}\sigma^{\text{aux}}_{11} + \frac{\kappa(\boldsymbol{x})-3}{8\mu(\boldsymbol{x})}\sigma^{\text{aux}}_{22}, \tag{45}$$

for the auxiliary fields. Substituting Eqs. (43)–(45) into Eq. (42), one obtains

$$M_{\text{local}} = -\lim_{\Gamma_s\to 0}\int_{\Gamma_s}\sigma^{\text{aux}}_{ij}n_j u_{i,1}\,\mathrm{d}\Gamma = -\frac{T}{E'_{\text{tip}}}\lim_{\Gamma_s\to 0}\int_{\Gamma_s}\sigma^{\text{aux}}_{ij}n_j\,\mathrm{d}\Gamma. \tag{46}$$

Because the force f is in equilibrium (see Fig. 2)

$$f = -\lim_{\Gamma_s\to 0}\int_{\Gamma_s}\sigma^{\text{aux}}_{ij}n_j\,\mathrm{d}\Gamma \tag{47}$$

and thus the following relationship is obtained

$$T = \frac{E'_{\text{tip}}}{f}M_{\text{local}}, \tag{48}$$

where $E'_{\text{tip}} = E_{\text{tip}}$ for generalized plane stress and $E_{\text{tip}}/(1-\nu^2_{\text{tip}})$ for plane strain. Notice that both the T and the SIF formulations are applicable to FGMs by virtue of the incompatible formulation adopted for the auxiliary strain fields (see Section 2), which provides the framework for the present unified approach.

6. Some micromechanics models

Various micromechanics models have been developed to evaluate effective properties in statistically homogeneous materials. The central assumption in classical micromechanics models is the existence of a representative volume element (RVE) [39,40] at each point within the heterogeneous continuum. Because the concept of an RVE loses its uniqueness for FGMs which has statistically inhomogeneous materials due to nonuniform reinforcement phases, such assumption is questionable in the FGM case [41]. To overcome limitations of RVE-based micromechanics models, Aboudi et al. [41,42] have developed a higher-order micromechanical theory which couples local and global effects. On the other hand, Zuiker and Dvorak [43], Reiter et al. [44], and Reiter and Dvorak [45] have claimed that the self-consistent and MT may be used to estimate the effective properties of graded materials with reasonable accuracy. Thus, we investigate the self-consistent [46–49] and the MT [50]. These estimates are bounded by the classical Hashin–Shtrikman bounds [51]. These methods provide the shear (μ) and bulk (κ) moduli of the graded composite. Based on these quantities, the corresponding Young's modulus and Poisson's ratio of the material are readily obtained by the following elasticity relations

$$E = \frac{9\mu\kappa}{\mu+3\kappa}, \qquad \nu = \frac{3\kappa-2\mu}{2(\mu+3\kappa)}. \tag{49}$$

6.1. Hashin–Shtrikman bounds

Hashin and Shtrikman [51] derived upper and lower bounds for the effective elastic moduli of quasi-isotropic and quasi-homogeneous multiphase materials of arbitrary phase geometry by means of variational

principles using the linear theory of elasticity and the elastic polarization tensor. For two-phase materials, the bounds on the effective shear and bulk moduli are [51]:

$$\begin{aligned}
\mu_1^e &= \mu_1 + V_2 \Bigg/ \left[\frac{1}{\mu_2 - \mu_1} + \frac{6(\kappa_1 + 2\mu_1)V_1}{5\mu_1(3\kappa_1 + 4\mu_1)} \right], \\
\mu_2^e &= \mu_2 + V_1 \Bigg/ \left[\frac{1}{\mu_1 - \mu_2} + \frac{6(\kappa_2 + 2\mu_2)V_2}{5\mu_2(3\kappa_2 + 4\mu_2)} \right], \\
\kappa_1^e &= \kappa_1 + V_2 \Bigg/ \left[\frac{1}{\kappa_2 - \kappa_1} + \frac{3V_1}{(3\kappa_1 + 4\mu_1)} \right], \\
\kappa_2^e &= \kappa_2 + V_1 \Bigg/ \left[\frac{1}{\kappa_1 - \kappa_2} + \frac{3V_2}{(3\kappa_2 + 4\mu_2)} \right],
\end{aligned} \tag{50}$$

where $\kappa_2^e > \kappa_1^e$, $\mu_2^e > \mu_1^e$, the superscript e denotes the effective quantity, V_1 and V_2 are the volume fractions of phases 1 and 2, respectively, μ_1 and μ_2 are the shear moduli of phases 1 and 2, respectively, and κ_1 and κ_2 are the bulk moduli of phases 1 and 2, respectively.

6.2. Self-consistent method

The self-consistent method (SCM) was derived to estimate the elastic properties of single-phase polycrystalline materials. A typical crystal is viewed as a spherical or ellipsoidal inclusion embedded in an infinite medium with the unknown isotropic properties of the polycrystal, and this system is subjected to uniform stress or strain conditions at large distances from the inclusion. For self-consistency, the orientation average of the stress or strain in the inclusion is set equal to the overall stress or strain.

For a two-phase composite, the shear and bulk moduli (μ, κ) are given as [49]:

$$\frac{1}{\kappa + \frac{4}{3}\mu} = \frac{V_1}{\kappa_1 + \frac{4}{3}\mu} + \frac{V_2}{\kappa_2 + \frac{4}{3}\mu}, \tag{51}$$

$$\left(\frac{V_1\kappa_1}{\kappa_1 + \frac{4}{3}\mu} + \frac{V_2\kappa_2}{\kappa_2 + \frac{4}{3}\mu} \right) + 5\left(\frac{V_1\mu_2}{\mu - \mu_2} + \frac{V_2\mu_1}{\mu - \mu_1} \right) + 2 = 0, \tag{52}$$

where V_1 and V_2 are the volume fractions of phases 1 and 2, respectively. After solving the above coupled equations for μ and κ, one obtains the Young's modulus E and the Poisson's ratio v of the graded composite by means of Eq. (49).

6.3. Mori–Tanaka method

The MT also uses the average local stress and strain fields of the constituents of the composite to estimate the effective material properties. The MT is essentially mathematical and it involves complex manipulations of the field variables and special concepts of eigenstrain and backstress. For spherical inclusion under nondilute conditions, it yields the same expressions as the Hashin–Shtrikman lower bounds, i.e. μ_1^e and κ_1^e given by Eq. (50) [50]. Again, the Young's modulus E and the Poisson's ratio v of the graded composite are obtained by using Eq. (49).

7. Maximum hoop stress criterion incorporating T-stress

The generalized maximum hoop stress criterion [4,5,19] was introduced to incorporate T-stress effect into the conventional maximum hoop stress criterion for homogeneous materials. Due to the local nature of the

criterion, the basic formulation for FGMs is the same as that for homogeneous materials. The asymptotic stresses for linear elastic isotropic FGMs are given in polar coordinates as:

$$\begin{aligned}
\sigma_{rr} &= \frac{1}{\sqrt{2\pi r}}\cos\frac{\theta}{2}\left[K_{\mathrm{I}}\left(1+\sin^2\frac{\theta}{2}\right)+\frac{3}{2}K_{\mathrm{II}}\left(\sin\theta-2\tan\frac{\theta}{2}\right)\right]+T\cos^2\theta,\\
\sigma_{\theta\theta} &= \frac{1}{\sqrt{2\pi r}}\cos\frac{\theta}{2}\left[K_{\mathrm{I}}\cos^2\frac{\theta}{2}-\frac{3}{2}K_{\mathrm{II}}\sin\theta\right]+T\sin^2\theta,\\
\sigma_{r\theta} &= \frac{1}{2\sqrt{2\pi r}}\cos\frac{\theta}{2}\left[K_{\mathrm{I}}\sin\theta+K_{\mathrm{II}}(3\cos\theta-1)\right]-T\sin\theta\cos\theta,
\end{aligned} \tag{53}$$

where K_{I}, K_{II} and T denote the mixed-mode SIFs and T-stress, respectively. The conventional maximum hoop stress criterion was proposed for brittle materials by Erdogan and Sih [1]. They postulated that the crack will grow in the direction along which the maximum hoop stress $\sigma_{\theta\theta}$ occurs and the shear stress $\sigma_{r\theta}$ is zero. Therefore the crack initiation angle θ_0 is obtained from

$$\partial\sigma_{\theta\theta}/\partial\theta = 0 \Rightarrow \theta = \theta_0. \tag{54}$$

Substitution of $\sigma_{\theta\theta}$ from Eq. (53) into Eq. (54) leads to [19]

$$\cos\frac{\theta_0}{2}\left[K_{\mathrm{I}}\sin\theta_0+K_{\mathrm{II}}(3\cos\theta_0-1)-\frac{16}{3}T\sqrt{2\pi r_c}\sin\frac{\theta_0}{2}\cos\theta_0\right]=0, \tag{55}$$

where r_c is an additional length scale representing the fracture process zone size. The crack initiation angle is evaluated by means of Eq. (55). For instance, for an inclined center crack in a homogeneous plate subjected to far-field constant traction as shown in Fig. 5, the closed-form solutions for SIFs and T-stress are given by [19]

$$\begin{aligned}
K_{\mathrm{I}} &= \sigma\sqrt{\pi a}(\lambda\cos^2\alpha+\sin^2\alpha),\\
K_{\mathrm{II}} &= \sigma\sqrt{\pi a}(1-\lambda)\sin\alpha\cos\alpha,\\
T &= \sigma(1-\lambda)\cos 2\alpha.
\end{aligned} \tag{56}$$

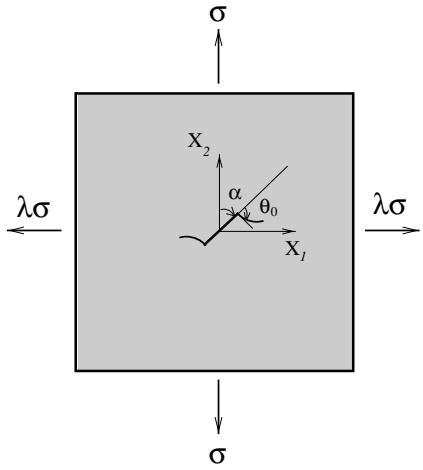

Fig. 5. An inclined center crack in a biaxially loaded homogeneous plate with crack angle α and crack initiation angle θ_0.

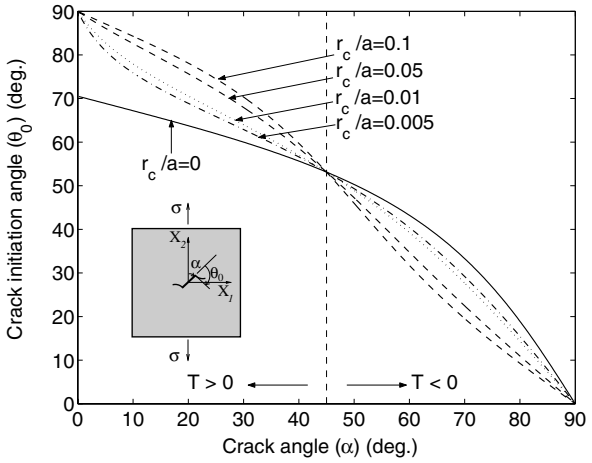

Fig. 6. Crack initiation angle predicted by generalized maximum hoop stress criterion $(M(\sigma_{\theta\theta})_{\max})$ for an inclined center crack in a homogeneous plate under far-field axial loading.

Fig. 6 plots the crack initiation angles versus crack angles for various critical distances r_c by using Eq. (55). Notice that the positive T-stress increases the crack initiation angle for $0^\circ \leqslant \theta \leqslant 45^\circ$, while the negative T-stress decreases the crack initiation angle for $45^\circ \leqslant \theta \leqslant 90^\circ$.

Once the crack initiation angle is determined, the crack initiation condition is obtained by considering the critical hoop stress $(\sigma_{\theta\theta})_c$ at the distance r_c. Then [19]

$$\sqrt{2\pi r_c}(\sigma_{\theta\theta})_c = \cos\frac{\theta_0}{2}\left[K_{\mathrm{I}}\cos^2\frac{\theta_0}{2} - \frac{3}{2}K_{\mathrm{II}}\sin\theta_0\right] + \sqrt{2\pi r_c}T\sin^2\theta_0. \tag{57}$$

For pure mode I when K_{II}, θ_0, and T are all equal to zero, K_{I} can be replaced by the mode I fracture toughness K_{Ic}. Therefore

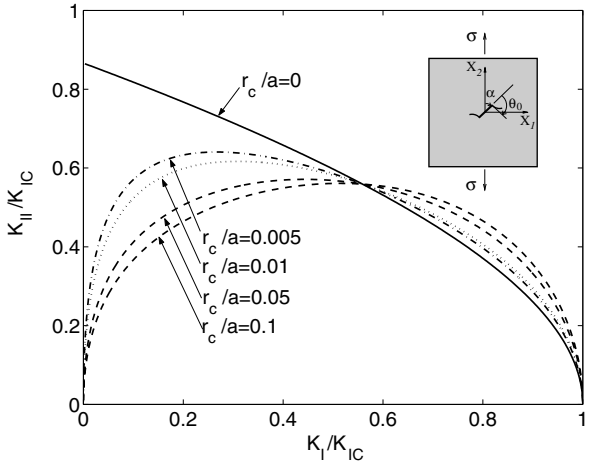

Fig. 7. Fracture loci predicted by generalized maximum hoop stress criterion $(M(\sigma_{\theta\theta})_{\max})$ for an inclined center crack in a homogeneous plate under far-field axial loading.

$$\sqrt{2\pi r_c}(\sigma_{\theta\theta})_c = K_{Ic}. \tag{58}$$

Substitution $\sigma_{\theta\theta}$ of Eq. (58) into Eq. (57) yields the crack initiation condition [19]:

$$\cos\frac{\theta_0}{2}\left[K_I\cos^2\frac{\theta_0}{2} - \frac{3}{2}K_{II}\sin\theta_0\right] + \sqrt{2\pi r_c}T\sin^2\theta_0 = K_{Ic}. \tag{59}$$

The fracture locus can be obtained by using Eqs. (55) and (59). For the inclined center crack in a homogeneous plate subjected to far-field constant traction, Fig. 7 shows the fracture loci K_{II}/K_{Ic} versus K_I/K_{Ic} for various critical distances r_c.

8. FEM implementation

The I-FRANC2D (Illinois-FRANC2D) computer code has been used as the basic platform for the implementation and to obtain the results described in this paper. It is based on the FRANC2D (FRacture ANalysis Code 2D) [52,53], which was originally developed at Cornell University. The extended capabilities of I-FRANC2D consist of graded elements to discretize nonhomogeneous materials, and fracture parameters such as SIFs and T-stress for predicting crack initiation angle by means of a fracture criterion such as the generalized maximum hoop stress criterion. Although not described in the present work, quasi-static propagation in brittle FGMs can be accomplished by means of a remeshing strategy.

The graded elements, which are based on the *generalized isoparametric formulation* (GIF) [11], are used in this work and, in general, they show superior performance to conventional homogeneous elements (constant element-wise material property) [54]. Recently, Paulino and Kim [55] have performed the weak patch test for graded elements by assessing both *consistency* and *stability*. They also performed eigen-analysis at the element level and found that the eigenvalues and eigenvectors of graded elements may differ substantially from those of conventional homogeneous elements [55]. Using graded elements, the code can evaluate the SIFs and T-stress in FGMs by using the interaction integral [18] (M-integral) as well as a few more numerical schemes [11] such as the path-independent J_k^*-integral, the modified crack closure, and the displacement correlation technique. Based on previous numerical investigation [18], the interaction integral scheme provides good accuracy in comparison with the above-mentioned schemes. Thus the interaction integral is used in the present analysis. By means of this single approach, both SIFs and T-stress can be evaluated. Subsequently, these parameters are used to predict crack initiation angle in FGMs.

9. Examples

The performance of the interaction integral for evaluating SIFs and T-stresses in FGMs is examined by means of numerical examples. In order to assess the various features of the method, the following examples are presented:

1. Inclined center-crack in a plate.
   - Homogeneous plate under constant traction.
   - FGM plate under fixed-grip loading.
2. Edge-crack in a plate with hyperbolic-tangent materials.
3. Inclined center crack in a circular disk.
4. Edge-crack emanating from a semi-circular hole.
5. Crack in a multi-layered region.

Isoparametric graded elements are used to discretize all the geometry of the above examples. Singular quarter-point six-node triangles (T6qp) are used for crack-tip elements, eight-node serendipity elements (Q8) are used for a circular region around crack-tip elements and over most of the mesh, and regular six-node triangles (T6) are used in the transition zone between regions of Q8 elements. The FEM results reported consist of SIFs, T-stresses, and crack initiation angles obtained by means of the interaction integral in conjunction with the FEM.

The first example (number 1 above) is presented as a means to validate the implementation, and it consists of two parts. The first part has analytical closed-form solutions for SIFs, T-stress, and crack initiation angle, and it is investigated for an inclined center crack in a homogeneous finite plate ($a/W = 0.1$), which approximates an infinite domain. The second part of the first example is investigated both for an FGM plate with exponentially graded material properties, and for materials determined by the self-consistent model. The FEM results for T-stresses for an FGM plate with exponentially graded materials are compared with reference solutions obtained by means of the singular integral equation method by Paulino and Dong [56]. Thus the first example provides reference solutions for crack initiation angles in FGMs. The second example makes use of hyperbolic-tangent materials, which can model various material properties such as homogeneous, "bi-material", and smoothly varying FGM. The third example investigates an inclined center crack in a circular disk with exponentially radially-graded materials. The fourth example deals with the effect of material nonhomogeneity on the crack initiation angle for an edge-crack emanating from a semi-circular hole. Finally, the fifth example investigates the effects of either an edge crack or an interior crack in a multi-layered region.

9.1. Inclined center-crack in a plate

Fig. 8(a) shows an inclined center-crack of length $2a$ located with angle α (clockwise) in a homogeneous plate under constant traction, and Fig. 8(b) shows an inclined center-crack of length $2a$ located with angle α (clockwise) in an FGM plate under fixed-grip loading. Fig. 8(c) shows the complete mesh configuration used for both cases, and Fig. 8(d) shows the mesh detail using 12 sectors (S12) and 4 rings (R4) of elements around the crack tips. The displacement boundary condition is prescribed such that $u_2 = 0$ along the lower edge and $u_1 = 0$ for the node at the left hand side. The mesh discretization consists of 1641 Q8, 94 T6, and 24 T6qp elements, with a total of 1759 elements and 5336 nodes. The following data were used for the FEM analysis: $a/W = 0.1$; $L/W = 1.0$; $\alpha = (0\text{–}90^\circ)$; generalized plane stress; and 2×2 Gauss quadrature. Such data are common to both problems (i.e. Parts 1 and 2 in Fig. 8) which are presented next.

9.1.1. Homogeneous plate under constant traction

This example has analytical solutions and consists of an inclined center crack in a homogeneous plate is subjected to far-field constant traction. Young's modulus and Poisson's ratio are $E = 1.0$ and $v = 0.3$, respectively. The applied loads correspond to $\sigma_{22}(X_1, 10) = \sigma = 1.0$ (see Fig. 8(a)). For this case, the closed-form solutions for SIFs and T-stress are given by [19]

$$K_{\mathrm{I}} = \sigma\sqrt{\pi a}\sin^2\alpha, \quad K_{\mathrm{II}} = \sigma\sqrt{\pi a}\sin\alpha\cos\alpha, \quad T = \sigma\cos 2\alpha. \tag{60}$$

Fig. 9 shows comparison of the present FEM results for crack initiation angles with those obtained by closed-form solutions (Eq. (60)), predicted by generalized maximum hoop stress criterion $(M(\sigma_{\theta\theta})_{\max})$ for $r_c/a = 0$ and 0.01. Notice that the FEM results for crack initiation angles agree well with those obtained by the closed-form solutions. Table 1 shows the quantitative comparison between FEM results and closed-form solutions for SIFs and T-stresses for an inclined center crack under constant traction, and indicates good agreement between the two types of solutions.

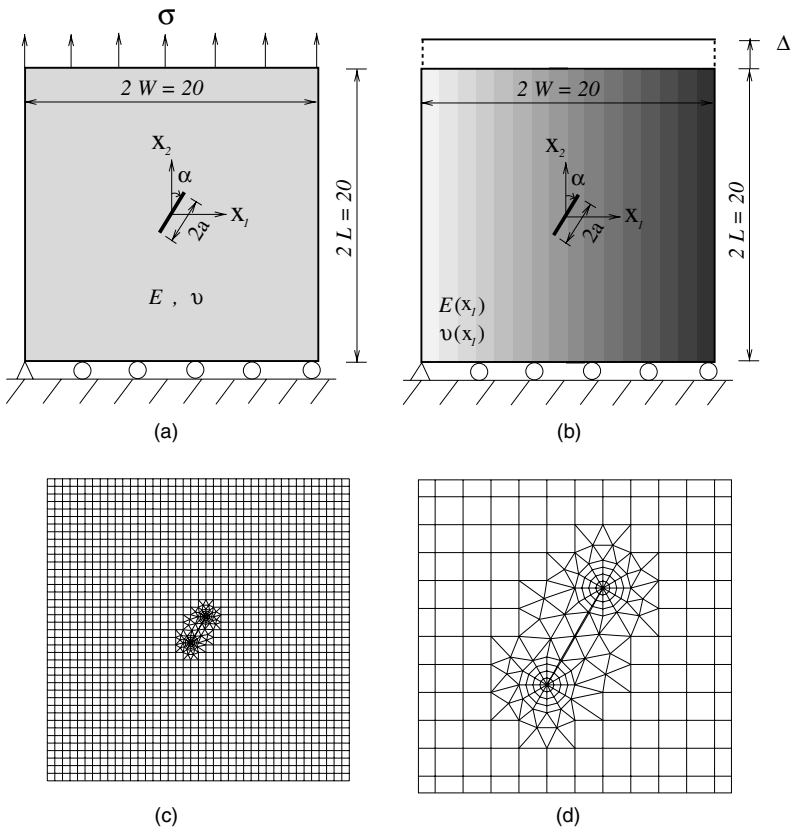

Fig. 8. Example 1: plate with an inclined crack of angle α. (a) Part 1: geometry and BCs with constant traction; (b) Part 2: geometry and BCs with fixed-grip loading; (c) complete finite element mesh; (d) mesh detail with 12 sectors (S12) and 4 rings (R4) around the crack tips ($\alpha = 30°$ clockwise).

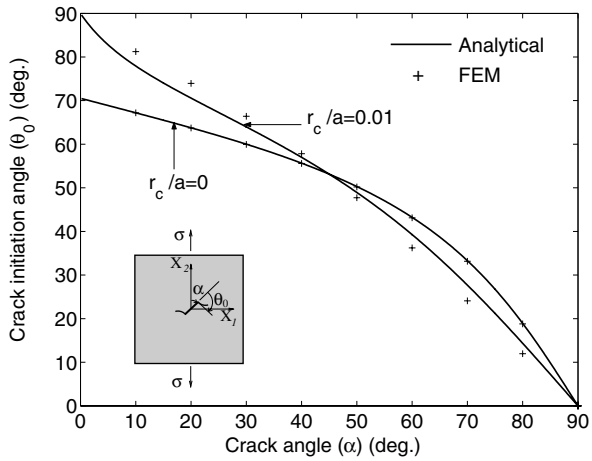

Fig. 9. Example 1, Part 1: comparison of FEM results (denoted by +) for crack initiation angles with those obtained by closed-form solutions (solid lines), which are predicted by generalized maximum hoop stress criterion $(M(\sigma_{\theta\theta})_{\max})$ for an inclined center crack in a homogeneous plate under constant traction.

Table 1
Example 1, Part 1: comparison of FEM results for SIFs and T-stresses with closed-form solutions for an inclined center crack in a homogeneous plate under far-field constant traction (see Fig. 8(a))

α (deg)	FEM			Exact		
	K_I	K_{II}	T	K_I	K_{II}	T
0	0.000	0.000	0.995	0.000	0.000	1.000
10	0.054	0.305	0.934	0.053	0.303	0.939
20	0.210	0.574	0.759	0.207	0.569	0.766
30	0.448	0.773	0.493	0.443	0.767	0.500
40	0.741	0.878	0.167	0.732	0.872	0.173
50	1.052	0.878	−0.179	1.040	0.872	−0.173
60	1.343	0.771	−0.508	1.329	0.767	−0.500
70	1.581	0.571	−0.773	1.565	0.569	−0.766
80	1.735	0.304	−0.947	1.719	0.303	−0.939
90	1.788	0.000	−1.007	1.772	0.000	−1.000

9.1.2. FGM plate under fixed-grip loading

This example makes use of either exponential gradation or material gradation determined by means of the self-consistent model. While the first material gradation consists of a closed-form expression for the material properties, the second one provides discrete values of the material properties as given by Eq. (49). The finite element analyses for SIFs, T-stresses, and crack initiation angles for both types of material gradation are performed for every 5° of crack angle from 5° to 90°. Since the solutions for 0° are not plausible, the crack angle 1° is chosen.

For exponentially graded materials, Paulino and Dong [56] evaluated T-stress by using a special integral equation method. In their analysis, Young's modulus is an exponential function of X_1, while Poisson's ratio is constant. Fig. 10 shows the variation of Young's modulus given by

$$E(X_1) = \overline{E}e^{\beta X_1}. \tag{61}$$

The following data were used: $\nu = 0.3$, $\overline{E} = 1.0$, $\beta a = (0.0, 0.25, 0.5, 1.0)$. The applied load corresponds to $\sigma_{22}(X_1, 10) = \bar{\varepsilon}\overline{E}e^{\beta X_1}$ with $\bar{\varepsilon} = 1.0$ (see Fig. 8(b)). This loading results in a uniform strain $\varepsilon_{22}(X_1, X_2) = \bar{\varepsilon}$ in a corresponding uncracked structure.

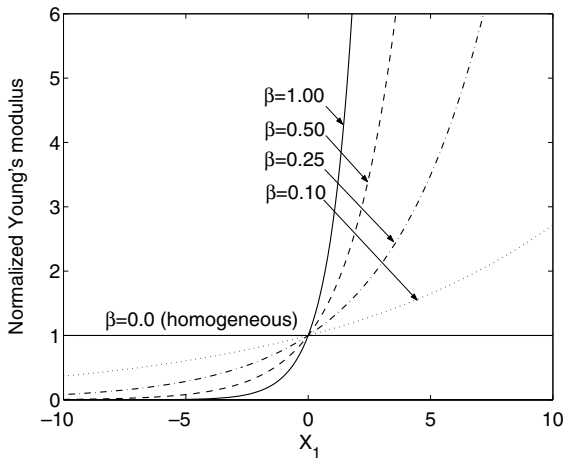

Fig. 10. Example 1, Part 2: variation of normalized Young's modulus ($E(X_1)/\overline{E}$) with position.

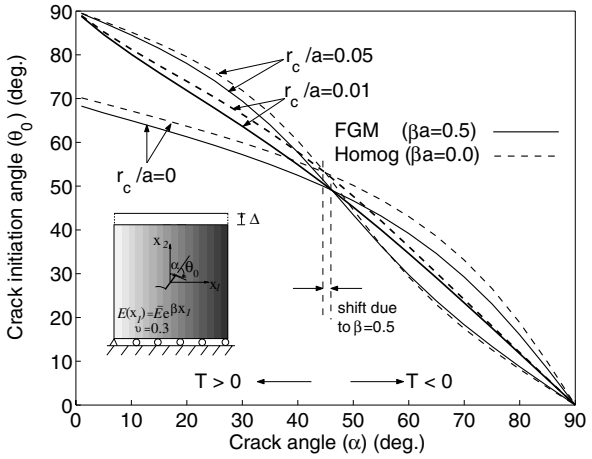

Fig. 11. Example 1, Part 2: the FEM results for crack initiation angles predicted by generalized maximum hoop stress criterion $M(\sigma_{\theta\theta})_{\max}$) for an inclined center crack in an FGM plate under fixed-grip loading for $\beta a = 0.0$ and 0.5.

Fig. 11 shows the FEM results for crack initiation angles versus geometric crack angles for the right crack tip for both homogeneous and FGM cases. Notice that positive T-stress increases crack initiation angle for the crack angle less than about 45°, and negative T-stress decreases crack initiation angle for the crack angle more than about 45° for both homogeneous and FGM cases. Fig. 12 shows the FEM results for crack initiation angles versus geometric crack angles for the right crack tip for the FGM case with fixed $\beta a = 0.5$. Notice that T-stress, in conjunction with the ratio r_c/a, has a significant influence on the crack initiation angle, and that, as before, positive T-stress increases the crack initiation angle, while negative T-stress decreases the crack initiation angle. Notice also that when $r_c/a = 0.0$, there is no effect of T-stress. Fig. 13 shows the FEM results for crack initiation angles versus crack angles for the right crack tip for various βa with a fixed $r_c/a = 0.01$. Notice that there is not much effect of material nonhomogeneity for a nearly horizontal ($\alpha \approx 90°$) or a nearly vertical ($\alpha \approx 0°$) crack, however, such effect is more pronounced in

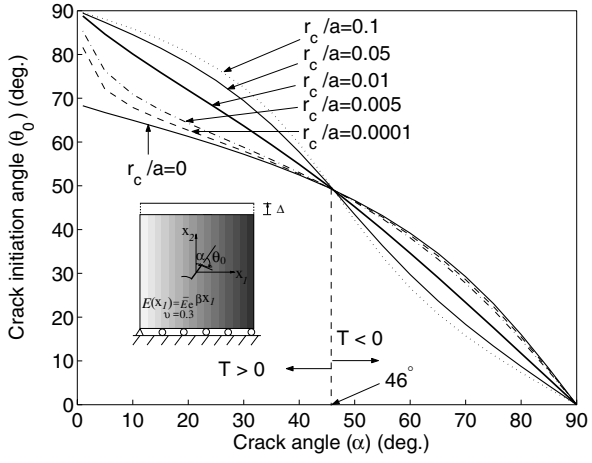

Fig. 12. Example 1, Part 2: the FEM results for crack initiation angle predicted by generalized maximum hoop stress criterion ($M(\sigma_{\theta\theta})_{\max}$) for an inclined center crack in an FGM plate under fixed-grip loading for various r_c/a values with $\beta a = 0.5$.

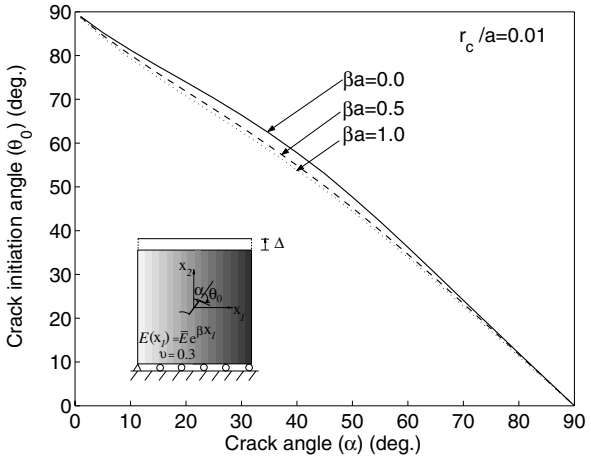

Fig. 13. Example 1, Part 2: the FEM results for crack initiation angles predicted by generalized maximum hoop stress criterion ($M(\sigma_{\theta\theta})_{\max}$) for an inclined center crack in an FGM plate under fixed-grip loading for various βa with fixed $r_c/a = 0.01$.

the mid-range of the plot (e.g. $10° < \alpha < 70°$). Table 2 shows the FEM results for SIFs, T-stresses, and crack initiation angles for an inclined center crack under fixed-grip loading for the homogeneous material case, i.e. $\beta a = 0.0$ (see Fig. 11). A comparison between Tables 1 and 3 reveal the influence of the loading boundary conditions (applied force versus applied displacement) on the SIFs and T-stress. Table 3 compares the FEM results for T-stress with the reference solutions obtained by Paulino and Dong [56] for both homogeneous ($\beta a = 0.0$) and nonhomogeneous ($\beta a \neq 0.0$) materials. Notice that the material nonhomogeneity is represented by the parameter βa, which is dimensionless. There is a reasonably good agreement between the present FEM results and the semi-analytical results of reference [56]. For both crack tips $(+a, -a)$, these results show that the T-stress changes sign for the crack angle $\alpha \approx 45°$ for $\beta a = 0.00$ and 0.25, however, the angle increases as βa increases, e.g. $\beta a = 0.50$ (cf. last two columns of Table 3). Table 4 shows the FEM results for SIFs, T-stresses, and crack initiation angles for an inclined center crack under fixed-grip loading for $\beta a = 0.5$ (see Fig. 11). For FGMs, the numerical results for SIFs, T-stresses, and crack initiation angles are different at the right and left crack tips because material gradation breaks down the symmetry achieved with homogeneous materials.

Table 2
Example 1, Part 2: SIFs, T-stresses, and crack initiation angles for an inclined center crack under fixed-grip loading for $\beta a = 0.0$, which refers to a homogeneous material (see Fig. 8(b))

α (deg)	K_I	K_{II}	T	θ_0 (deg)	
				$r_c/a = 0.00$	$r_c/a = 0.01$
0	0.000	0.000	0.995	–	–
10	0.054	0.305	0.933	68.8	85.2
20	0.209	0.570	0.758	67.1	81.2
30	0.446	0.768	0.491	65.4	77.5
40	0.735	0.869	0.165	63.6	73.9
50	1.039	0.865	−0.177	61.8	70.2
60	1.323	0.758	−0.497	59.9	66.4
70	1.552	0.560	−0.756	57.8	62.2
80	1.700	0.298	−0.924	55.5	57.7
90	1.752	0.000	−0.982	0.0	0.0

Table 3
Example 1, Part 2: comparison of FEM results for T-stresses with reference solutions [56] (see Fig. 8(b))

Method	α (deg)	$\beta a = 0.00$		$\beta a = 0.25$		$\beta a = 0.50$	
		$T(+a)$	$T(-a)$	$T(+a)$	$T(-a)$	$T(+a)$	$T(-a)$
Present	0	0.9950	0.9950	0.9949	0.9948	0.9946	0.9944
	15	0.8592	0.8592	0.8625	0.8569	0.8684	0.8505
	30	0.4912	0.4912	0.4992	0.4905	0.5146	0.4841
	45	−0.0055	−0.0055	−0.0077	−0.0019	0.0391	0.0109
	60	−0.4974	−0.4974	−0.4790	−0.4763	−0.4288	−0.4371
	75	−0.8534	−0.8534	−0.8310	−0.8191	−0.7655	−0.7494
	90	−0.9828	−0.9828	−0.9589	−0.9430	−0.8878	−0.8606
Paulino and Dong [56]	0	1.0000	1.0000	1.0000	1.0000	1.0000	1.0000
	15	0.8660	0.8660	0.8665	0.8643	0.8701	0.8585
	30	0.4999	0.5000	0.5024	0.4981	0.5132	0.4905
	45	0.0002	0.0000	0.0106	0.0048	0.0393	0.0109
	60	−0.5001	−0.5001	−0.4871	−0.4727	−0.4200	−0.4444
	75	−0.8660	−0.8660	−0.8266	−0.8316	−0.7483	−0.7631
	90	−0.9999	−0.9999	−0.9543	−0.9590	−0.8670	−0.8766

Table 4
Example 1, Part 2: the FEM results for SIFs, T-stresses, and crack initiation angles for an inclined center crack under fixed-grip loading for $\beta a = 0.5$ (see Fig. 8(b))

α (deg)	K_{I}^{+}	K_{II}^{+}	K_{I}^{-}	K_{II}^{-}	T^{+}	T^{-}	θ_0^{+} (deg)		θ_0^{-} (deg)	
							$r_c/a = 0.00$	$r_c/a = 0.01$	$r_c/a = 0.00$	$r_c/a = 0.01$
0	0.000	0.000	0.000	0.000	0.994	0.994	–	–	–	–
10	0.094	0.316	0.019	0.286	0.939	0.926	66.7	84.6	69.2	82.3
20	0.309	0.614	0.133	0.512	0.771	0.748	64.9	80.1	65.6	75.8
30	0.632	0.850	0.310	0.655	0.514	0.484	63.1	75.9	61.8	68.8
40	1.032	0.989	0.520	0.708	0.202	0.171	61.2	71.8	57.3	60.1
50	1.465	1.006	0.729	0.676	−0.125	−0.147	59.3	67.8	51.9	49.2
60	1.878	0.895	0.915	0.571	−0.428	−0.437	57.2	63.6	44.7	36.5
70	2.220	0.670	1.059	0.410	−0.673	−0.665	54.9	59.3	34.6	23.5
80	2.444	0.358	1.149	0.214	−0.832	−0.810	52.4	54.8	19.5	11.2
90	2.522	0.000	1.179	0.000	−0.887	−0.860	0.0	0.0	0.0	0.0

For materials determined by the self-consistent model, the shear (μ) and bulk (κ) moduli are first evaluated by solving both Eqs. (51) and (52) for a range of volume fractions, i.e. $0 \leqslant V_i \leqslant 1$ ($i = 1$ or 2), and then Young's modulus and Poisson's ratio are evaluated by means of Eq. (49). For the self-consistent model, we employ the material properties of an engineering Ti/TiB FGM specimen which has been tested experimentally by Carpenter et al. [57], and investigated using cohesive fracture analysis by Jin et al. [58]. Material properties of Ti/TiB FGM, and the volume fraction of Ti are used as follows:

$$E_{\mathrm{TiB}} = 375\ \mathrm{GPa}, \quad \nu_{\mathrm{TiB}} = 0.14, \quad E_{\mathrm{Ti}} = 107\ \mathrm{GPa}, \quad \nu_{\mathrm{Ti}} = 0.34,$$
$$V_{\mathrm{Ti}}(X_1) = [(X_1 + 10)/(2W)]^{0.84} \quad (-10 \leqslant X_1 \leqslant 10),$$

respectively, where $2W$ is the gradation length, i.e. the width of the FGM plate (see Fig. 8(b)). The power $p = 0.84$ was obtained by Jin et al. [58] using a least square of the actual material distribution. However, the geometrical configuration adopted here differs significantly from those used by Carpenter et al. [57] and Jin et al. [58]. Young's modulus and Poisson's ratio determined by micromechanics models are shown in

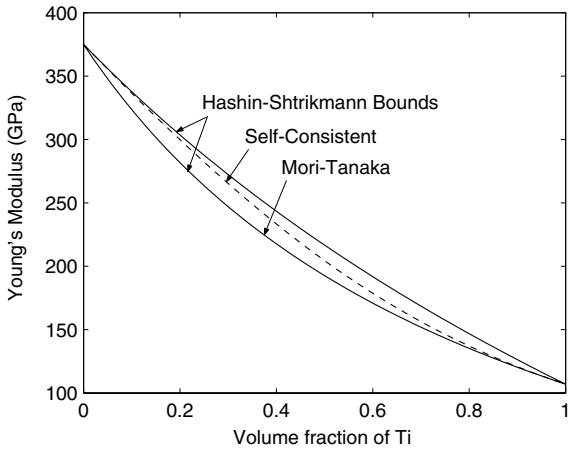

Fig. 14. Example 1, Part 2: variation of Young's modulus versus volume fraction of Ti according to micromechanics models for composites.

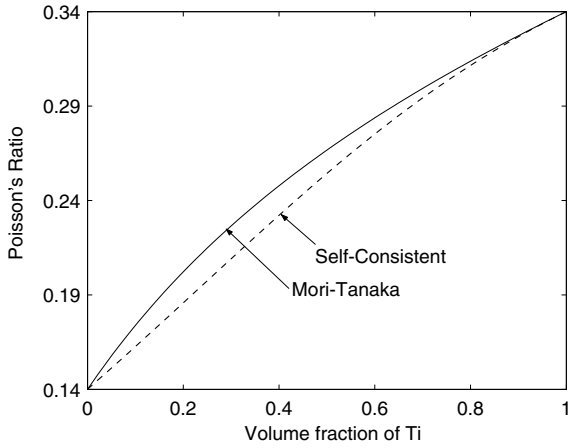

Fig. 15. Example 1, Part 2: variation of Poisson's ratio versus volume fraction of Ti according to micromechanics models for composites.

Figs. 14 and 15, respectively. The applied load is a uniform strain $\varepsilon_{22}(X_1, X_2) = \bar{\varepsilon} = 0.0005$ in a corresponding uncracked structure.

Fig. 16 shows the present FEM results for crack initiation angles versus crack angles for the right crack tip. As expected, the positive T-stress increases the crack initiation angle, while the negative T-stress decreases the crack initiation angle. Table 5 shows FEM results for SIFs, T-stresses, and crack initiation angles for an inclined center crack under fixed-grip loading (see Fig. 16). Notice that SIFs, T-stresses, and crack initiation angle are very similar at both crack tips, while such similarity was not observed for exponentially graded material. This is due to the fact that, for the specific choice of material in this example, the material variation, between the crack tips, obtained by the self-consistent model is smoother than that for the exponentially graded material. Moreover, Young's modulus is a descending function of position for the micromechanics model case and it is an ascending function of position for the exponentially graded case.

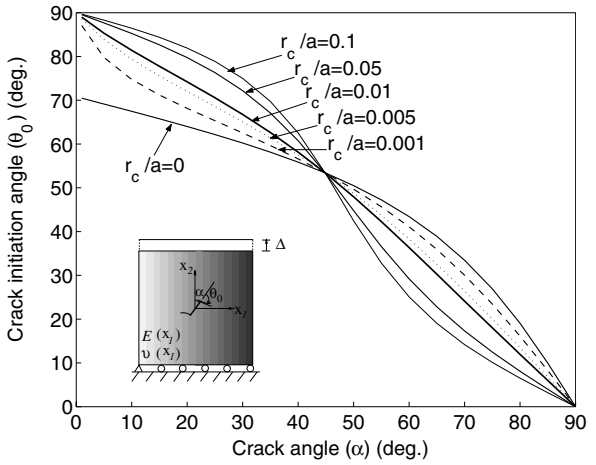

Fig. 16. Example 1, Part 2: the FEM results for crack initiation angles predicted by generalized maximum hoop stress criterion ($M(\sigma_{\theta\theta})_{\max}$) for an inclined center crack in a plate with FGMs determined by the *self-consistent model*.

Table 5
Example 1, Part 2: the FEM results for SIFs, T-stresses, and crack initiation angles for an inclined center crack under fixed-grip loading for FGMs determined by the self-consistent model (see Fig. 8(b))

α (deg)	K_{I}^{+}	K_{II}^{+}	K_{I}^{-}	K_{II}^{-}	T^{+}	T^{-}	θ_0^+ (deg)		θ_0^- (deg)	
							$r_c/a = 0.00$	$r_c/a = 0.01$	$r_c/a = 0.00$	$r_c/a = 0.01$
0	0.000	0.000	0.000	0.000	92.41	92.41	–	–	–	–
10	4.567	28.15	5.491	28.48	86.68	86.76	67.4	81.3	66.8	81.0
20	18.42	52.51	20.56	53.66	70.36	70.49	63.9	74.2	63.4	73.6
30	39.58	70.14	43.41	72.39	45.59	45.74	60.2	66.7	59.6	66.0
40	65.31	79.07	71.32	82.35	15.40	15.50	55.8	58.1	55.2	57.4
50	92.34	78.41	100.9	82.30	−16.37	−16.36	50.4	47.9	49.8	47.4
60	117.4	68.44	128.5	72.28	−45.97	−46.10	43.4	36.3	42.6	36.0
70	137.7	50.50	150.9	53.58	−69.88	−70.15	33.4	24.1	32.7	24.0
80	150.7	26.80	165.5	28.52	−85.44	−85.78	19.0	11.9	18.5	11.9
90	155.2	0.000	170.6	0.000	−90.82	−91.20	0.0	0.0	0.0	0.0

9.2. Edge crack in a plate with hyperbolic-tangent materials

This example investigates the influence of material gradation rotation and translation on SIFs, T-stresses, and crack initiation angles. Fig. 17(a) shows an edge crack of length a in a graded plate, and Fig. 17(b) shows the complete mesh discretization using 12 sectors (S12) and 4 rings (R4) of elements around the crack tip. Fig. 17(c)–(e) illustrate the three considered types of hyperbolic-tangent material gradation with respect to the crack tip: rotation, translation to the left, and translation to the right, respectively. The fixed-grip displacement loading is applied corresponding to $\sigma_{22}(X_1, 2) = \bar{\varepsilon}\overline{E}(X_1) = \bar{\varepsilon}E(X_1)/(1 - \nu^2)$, which results in a uniform strain $\varepsilon_{22}(X_1, X_2) = \bar{\varepsilon}$ in a corresponding uncracked structure. The displacement boundary condition is prescribed such that $u_2 = 0$ along the lower edge and $u_1 = 0$ for the node at the left hand side.

Young's modulus is a hyperbolic-tangent function which can be expressed with respect to the local (x_1, x_2) or global (X_1, X_2) Cartesian coordinates. For the rotation of material gradation,

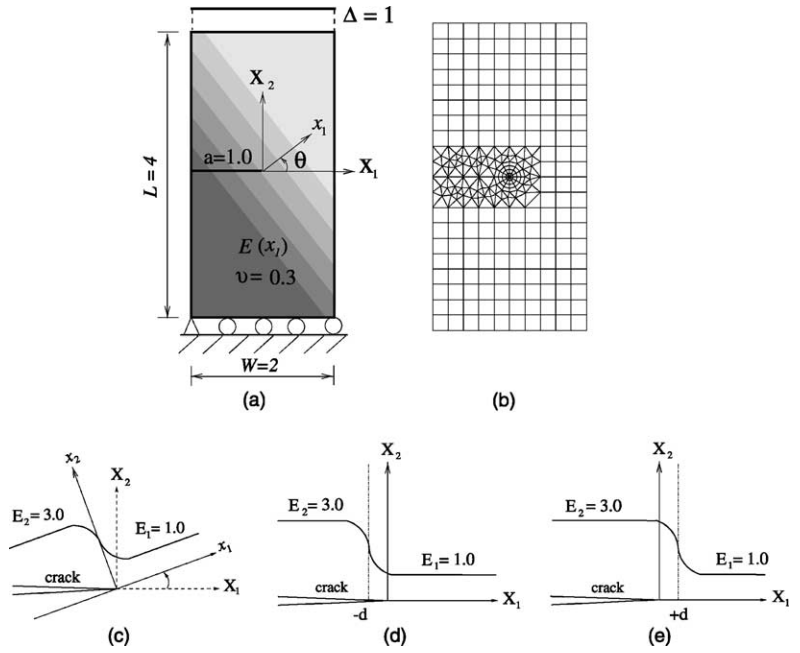

Fig. 17. Example 2: edge crack in a plate with hyperbolic-tangent materials: (a) geometry and BCs; (b) complete finite element mesh with 12 sectors (S12) and 4 rings (R4) around the crack tip; (c) rotation of material gradation with the angle θ; (d) translation of material gradation to the left ($d = 0.5$); (e) translation of material gradation to the right ($d = -0.5$).

$$E(x_1) = \frac{E_1 + E_2}{2} + \frac{E_1 - E_2}{2} \tanh(\beta(x_1)), \tag{62}$$

or, using global coordinates,

$$E(X_1, X_2) = \frac{E_1 + E_2}{2} + \frac{E_1 - E_2}{2} \tanh(\beta(X_1 \cos\theta + X_2 \sin\theta)). \tag{63}$$

For the translation of material gradation,

$$E(X_1) = \frac{E_1 + E_2}{2} + \frac{E_1 - E_2}{2} \tanh(\beta(X_1 + d)), \tag{64}$$

where d is a constant for translation. In this example, Poisson's ratio is taken as constant. The following data were used for the FEM analysis: $a/W = 0.5$; $L/W = 2.0$; $\beta a = 15.0$; $\bar{\varepsilon} = 0.25$; $(E_1, E_2) = (1.0, 3.0)$; $v = 0.3$; $d = (0, -0.5, 0.5)$; plane strain; and 2×2 Gauss quadrature. The mesh discretization consists of 208 Q8, 37 T6, and 12 T6qp elements, with a total of 257 elements and 1001 nodes.

Fig. 18 shows FEM results for crack initiation angle predicted by the generalized maximum hoop stress criterion for various rotations of material gradation θ, i.e. 0°–80°. Notice that T-stress (negative) decreases the crack initiation angle and it also decreases with the increasing r_c/a ratio. The gap between the curve for $r_c/a = 0$ (no T-stress effect) and the various curves for $r_c/a \neq 0$ (especially $r_c/a = 0.005$) indicate the significant influence of T-stress in the FGM case. If the material were homogeneous, then the crack initiation angle $\theta_0 = 0°$. Table 6 shows the FEM results for SIFs, T-stresses, and crack initiation angles in an edge crack for the rotation of hyperbolic-tangent material variation (see Fig. 17(c)). Table 7 shows FEM results for SIFs and T-stresses for the translation of hyperbolic-tangent material variation by considering

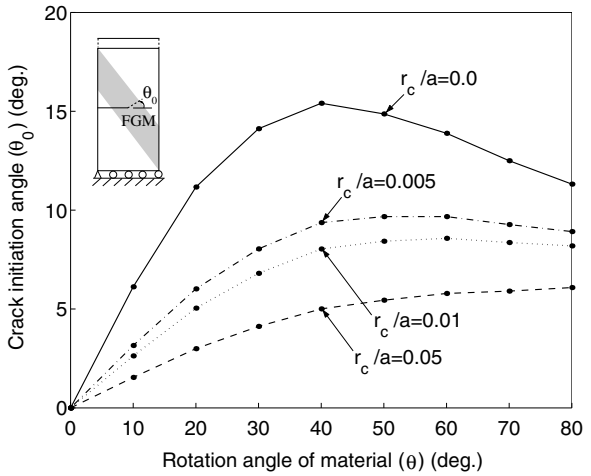

Fig. 18. Example 2: the FEM results for crack initiation angles predicted by generalized maximum hoop stress criterion ($M(\sigma_{\theta\theta})_{\max}$) for an edge crack in a plate with various rotations of hyperbolic-tangent materials under fixed-grip loading (see Fig. 17(c)).

Table 6
Example 2: the FEM results for SIFs, T-stresses, and crack initiation angles for an edge crack with various rotations of hyperbolic-tangent material variation (see Fig. 17(c))

θ (deg)	K_I	K_{II}	T	θ_0 (deg) ($r_c/a = 0.00$)	θ_0 (deg) ($r_c/a = 0.01$)
0	1.0190	0.0000	−1.176	0.00	0.00
10	0.9949	−0.0535	−1.128	6.12	2.62
20	0.9560	−0.0953	−1.015	11.16	5.04
30	0.8932	−0.1141	−0.859	14.11	6.80
40	0.8363	−0.1174	−0.696	15.40	8.03
50	0.7879	−0.1064	−0.545	14.86	8.42
60	0.7498	−0.0941	−0.418	13.88	8.57
70	0.7209	−0.0809	−0.318	12.50	8.36
80	0.6981	−0.0706	−0.236	11.31	8.19

Table 7
Example 2: the FEM results for SIFs and T-stress for an edge crack with translation (d) of hyperbolic-tangent material variation: (see Fig. 17(d) and (e))

Translation (d)	K_I	T
−0.5	1.163	−0.554
−0.3	1.167	−0.589
−0.1	1.190	−0.861
0.0	1.019	−1.176
0.1	0.582	−0.431
0.3	0.440	−0.211
0.5	0.410	−0.188

Notice that $K_{II} = 0$.

$d \in [-0.5, 0.5]$. Notice that T-stresses are all negative and the crack initiation angle is zero because of symmetry, i.e. $\theta = 0^\circ$ and $K_{II} = 0$, in the particular cases illustrated by Table 7.

9.3. Inclined center crack in a circular disk

Fig. 19(a)–(c) show a circular disk with a center crack inclined by $\theta = 30^\circ$ (with respect to the Cartesian X_1 axis), the complete mesh configuration, and the mesh detail around the crack tip using 12 sectors (S12) and 4 rings (R4), respectively. A point load is applied to the top and bottom nodes, i.e. $P(X_1, \pm 10) = \pm 100$. The displacement boundary condition is prescribed such that $(u_1, u_2) = (0, 0)$ for the node at $(X_1, X_2) = (-10, 0)$ and $u_2 = 0$ for the node at $(X_1, X_2) = (10, 0)$. Young's modulus is an exponential function of the radius r given by

$$E(r) = \overline{E}e^{\beta r}, \qquad r = \sqrt{X_1^2 + X_2^2}. \tag{65}$$

The following data were used for the FEM analysis: $a = 1$, $R = 10$; $\beta a = (-0.5 \text{ to } 0.5)$; $\overline{E} = 1.0$; $\nu = 0.3$; generalized plane stress; and 2×2 Gauss quadrature. The mesh discretization consists of 453 Q8, 228 T6, and 24 T6qp elements, with a total of 999 elements and 2712 nodes.

Fig. 20 shows the FEM results for crack initiation angles predicted by the generalized maximum hoop stress criterion for various values of the dimensionless material nonhomogeneity parameter βa. Due to symmetry of the radial material gradation, the values of SIFs and T-stress are the same at both crack tips (see Fig. 19(a)). Notice that the negative T-stress decreases the crack initiation angle (compare the curve for $r_c/a = 0$ with the other curves) and also the crack initiation angle decreases with the increasing r_c/a ratio. Table 8 shows the FEM results for SIFs, T-stresses, and crack initiation angles for various material nonhomogeneity βa. Notice that as βa increases, the mixed-mode SIFs decrease and the T-stress increases substantially. The sign of the T-stress is always negative for the range of material variation investigated.

9.4. Edge-crack emanating from a semi-circular hole

This example investigates the effect of material nonhomogeneity on SIFs, T-stress, and crack initiation angle for an edge-crack emanating from a semi-circle hole. Fig. 21(a)–(c) show an edge crack emanating from a semi-circle hole, the complete mesh configuration, and the mesh detail around the crack tip using 12 sectors (S12) and 4 rings (R4), respectively. The fixed-grip displacement loading is applied on the top edge, i.e. $\Delta(X_1, 5) = 10$. The displacement boundary condition is prescribed such that $(u_1, u_2) = (0, 0)$ for the left-bottom corner node and $u_2 = 0$ for the nodes on the bottom edge. The mesh discretization consists of 1142 Q8, 134 T6, and 12 T6qp elements, with a total of 1288 elements and 3903 nodes. Young's modulus is an exponential function of X_2, while Poisson's ratio is constant. The following data were used for the FEM

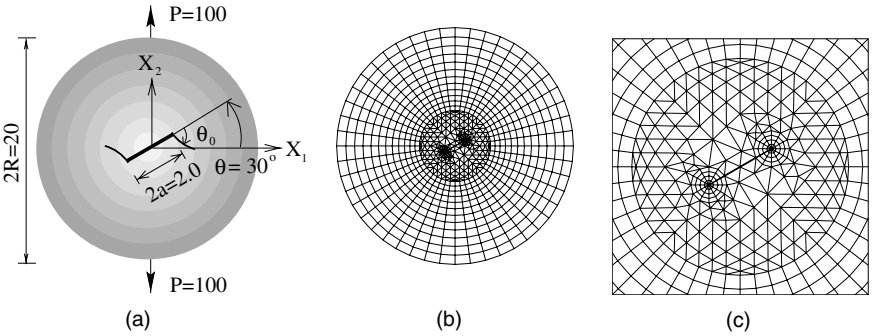

Fig. 19. Example 3: circular disk; (a) geometry and BCs for an inclined center crack; (b) the complete mesh configuration; (c) mesh detail with 12 sectors (S12) and 4 rings (R4) around the crack tip (S12, R4).

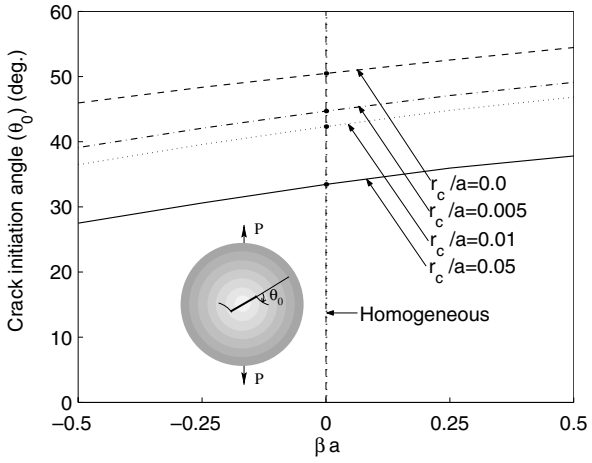

Fig. 20. Example 3: the FEM results for crack initiation angles predicted by generalized maximum hoop stress criterion ($M(\sigma_{\theta\theta})_{\max}$) for an inclined center crack in a disk subjected to a point load.

Table 8
Example 3: the FEM results for SIFs, T-stresses, and crack initiation angles for an inclined center crack in a circular disk (see Fig. 19)

β	K_{I}	K_{II}	T	θ_0 (deg) ($r_c/a = 0.00$)	θ_0 (deg) ($r_c/a = 0.01$)
−0.50	22.91	15.19	−13.08	45.9	36.4
−0.25	17.53	13.21	−9.93	48.3	39.5
0.00	11.47	9.74	−6.53	50.4	42.3
0.25	5.86	5.65	−3.49	52.5	44.8
0.50	2.20	2.42	−1.44	54.5	46.8

analysis: $a = 1.0$; $L = 10$, $W = 7$; $\overline{E} = 1.0$; $\beta a = (0.0\text{–}1.0)$; $v = 0.3$; generalized plane stress; and 2×2 Gauss quadature.

Fig. 22 shows the present FEM results for crack initiation angles predicted by the generalized maximum hoop stress criterion for various values of the material nonhomogeneity parameter βa. Notice that T-stress reduces the crack initiation angle and the crack initiation angle decreases with the increasing r/a ratio. It is expected that the crack initiation angle increases with the increasing material nonhomogeneity βa, while for homogeneous materials, the crack initiation angle is zero due to symmetry. Table 9 shows the FEM results for SIFs, T-stresses, and crack initiation angles for an edge crack emanating from a semi-circle hole. As βa deviates from zero and increases, mode I condition breaks down with the loss of symmetry and thus mode II behavior becomes more significant. Notice that the sign change for the T-stress occurs at $\beta a \approx 0.7$.

9.5. Crack in a multi-layered region

This example investigates a crack in a multi-layered region which includes two homogeneous materials and an FGM region in bewteen those two regions. This example is similar to those investigated by Ambrico et al. [59], who investigated thin multi-layers comprised of repeating patterns of different material sections, such as interconnect-dielectric structures in microelectronics. The material gradation for the FGM region has various ratios of Young's modulus. Fig. 23(a) and (b) show edge and interior cracks in a multi-layered region, respectively. Fig. 23(c)–(e) show the complete mesh configuration, the mesh detail around the top

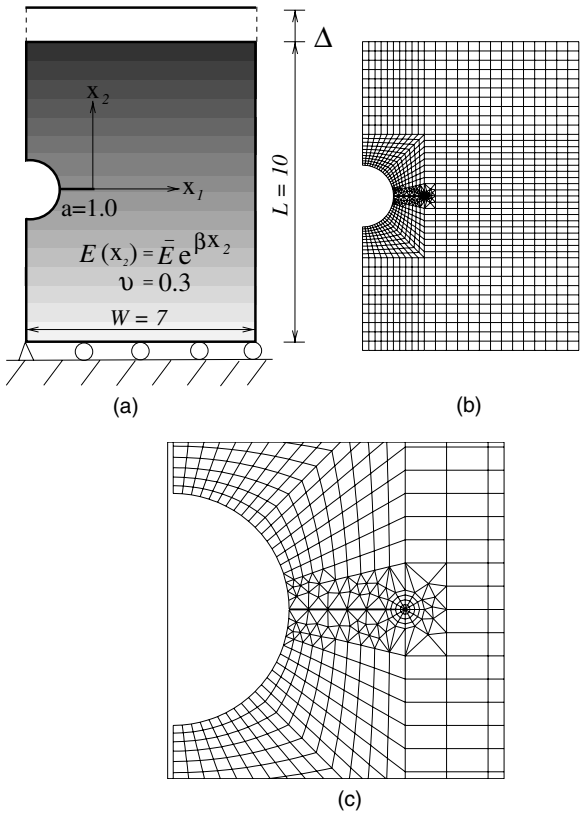

Fig. 21. Example 4: edge crack emanating from a semi-circle hole; (a) geometry and BCs; (b) the complete mesh configuration; (c) mesh detail with 12 sectors (S12) and 4 rings (R4) around the crack tip (S12, R4).

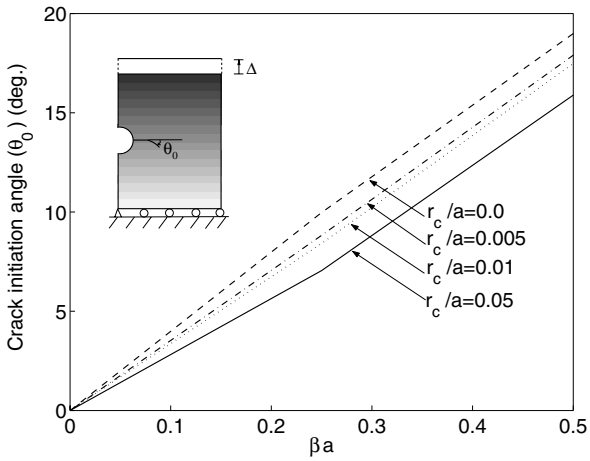

Fig. 22. Example 4: the FEM results for crack initiation angles predicted by generalized maximum hoop stress criterion ($M(\sigma_{\theta\theta})_{\max}$) for an edge crack emanating from a semi-circular hole.

Table 9
Example 4: the FEM results for SIFs, mode mixity (K_I/K_{II}), T-stresses, and crack initiation angles for an edge crack emanating from a semi-circular hole (see Fig. 21)

βa	K_I	K_{II}	K_{II}/K_I	T	θ_0 (deg) ($r_c/a = 0.00$)	θ_0 (deg) ($r_c/a = 0.01$)
0.00	2.208	0.000	0.000	−0.427	0.0	0.0
0.25	1.917	0.169	0.088	−0.311	9.9	8.4
0.50	1.310	0.232	0.177	−0.112	18.9	17.4
0.70	0.849	0.206	0.242	−0.0007	24.8	24.7
0.75	0.750	0.194	0.258	0.008	26.0	26.2
1.00	0.378	0.124	0.328	0.042	31.0	33.7

edge, and the mesh detail around the crack tip using 12 sectors (S12) and 4 rings (R4), respectively. The fixed-grip displacement loading is applied on the right edge, i.e. $\Delta(10, X_2) = 10$. The displacement boundary condition is prescribed such that $(u_1, u_2) = (0, 0)$ for the left-bottom corner node and $u_1 = 0$ for the nodes on the left edge. The mesh discretization consists of 1938 Q8, 96 T6, and 12 T6qp elements, with a total of 2046 elements and 5705 nodes. Young's modulus is constant for the top and bottom (substrate) homogeneous materials, and it is a linear function of X_2 in the FGM region, while Poisson's ratio is constant. The following data were used for the FEM analysis: $a = 1.0$; $L = 20$, $H = 100$; $E_1/E_2 = (0.1, 0.5, 0.75, 1.0, 2.0, 10.0)$; $\nu = 0.3$; $\bar{\varepsilon} = \Delta/L = 0.5$; plane strain; and 2×2 Gauss quadature.

Table 10 shows the FEM results for SIFs and T-stresses for edge and interior cracks in a multi-region plate. For an edge crack, the ratio E_2/E_1 has a significant effect on the T-stress as well as the mode I SIF. Notice that the T-stress changes sign from positive to negative as the ratio E_2/E_1 increases, and the sign changes between $E_2/E_1 = 0.1$ and $E_2/E_1 = 0.5$. For an interior crack, the T-stress remains negative for all the ratios of E_2/E_1 considered. For both cases, the mode I SIF increases and the T-stress decreases with an increasing ratio of E_2/E_1.

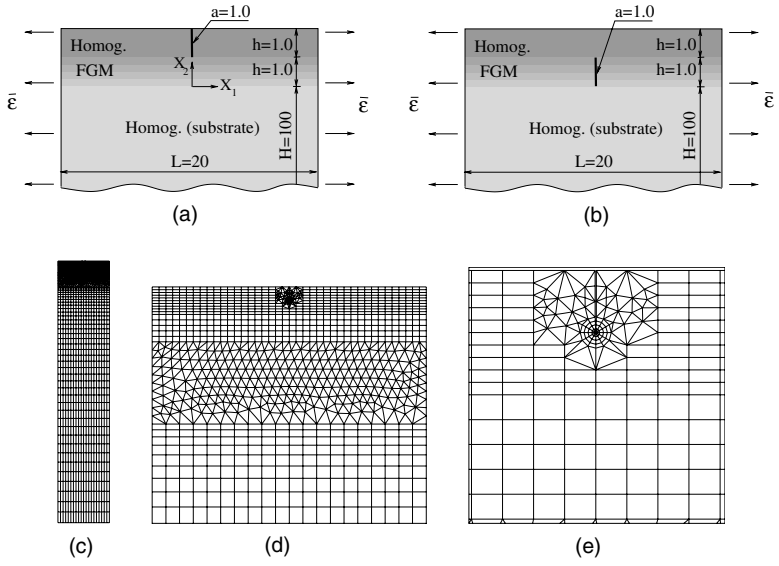

Fig. 23. Example 5: crack in a multi-layered region: (a) geometry and BCs with an edge crack; (b) geometry and BCs with an interior crack; (c) complete finite element mesh; (d) mesh detail around the top edge; (e) mesh detail around the crack tips with 12 sectors (S12) and 4 rings.

Table 10
Example 5: the FEM results for SIFs and T-stresses for edge and interior cracks in a multi-layered region

E_2/E_1	Edge crack		Interior crack			
	K_I	T	K_I^+	K_I^-	T^+	T^-
0.1	0.069	0.027	0.116	0.684	−0.156	−0.351
0.5	0.465	−0.115	0.383	0.674	−0.346	−0.461
0.75	0.748	−0.242	0.544	0.685	−0.458	−0.506
1	1.047	−0.382	0.706	0.700	−0.568	−0.546
2	2.333	−0.998	1.372	0.767	−0.988	−0.692
10	14.26	−6.538	7.346	1.274	−3.999	−1.768

The (+) and (−) denotes the upper crack tip of an interior crack, respectively (see Fig. 23).

10. Conclusions

This paper presents an accurate scheme for evaluating mixed-mode SIFs and T-stress by means of a unified approach using the interaction integral (M-integral) method considering arbitrarily oriented cracks in 2D elastic FGMs. The present interaction integral is accurate and efficient in dealing with any kind of smoothly varying material gradation including micromechanics models. Given SIFs and T-stress, a fracture criterion incorporating the T-stress effect can predict the crack initiation angle. From the numerical examples investigated, we observe that positive T-stress increases the crack initiation angle, and negative T-stress decreases the crack initiation angle. Moreover, the material gradation, which may be represented by the material nonhomogeneity parameter βa, has a significant influence on the magnitude and the sign of the T-stress. The direction of material gradation also shows a significant influence on SIFs, T-stress, and the crack initiation angles. The fracture criterion adopted here (generalized maximum hoop stress criterion) involves a physical length scale r_c, which is representative of the fracture process zone size. The length scale parameter may have a significant effect on the crack initiation angle, even with the same values of T-stress and SIFs. Therefore the parameter r_c must be carefully assessed by comparing numerical solutions with experimental results.

This paper provides a robust scheme for evaluating SIFs, T-stresses, and crack initiation angles in brittle FGMs. Potential extensions of the present work involve quasi-static crack propagation in brittle FGMs and plasticity considerations for crack propagation in ductile/brittle FGMs.

Acknowledgements

We would like to thank the support from NASA-Ames, Engineering for Complex Systems Program, and the NASA-Ames Chief Engineer (Dr. Tina Panontin) through grant NAG 2-1424. Additional support from the National Science Foundation (NSF) under grant CMS-0115954 (Mechanics & Materials Program) is also appreciated. Any opinions expressed herein are those of the writers and do not necessarily reflect the views of the sponsors.

References

[1] F. Erdogan, G.C. Sih, On the crack extension in plates under plane loading and transverse shear, ASME J. Basic Engrg. 85 (4) (1963) 519–527.

[2] M.A. Hussain, S.L. Pu, J. Underwood, Strain energy release rate for a crack under combined mode I and mode II, in: P.C. Paris, G.R. Irwin (Eds.), Fracture Analysis, ASTM STP560, American Society for Testing and Materials, Philadelphia, PA, 1993, pp. 2–28.

[3] G.C. Sih, Strain energy density factor applied to mixed mode crack problems, Int. J. Fract. 10 (3) (1974) 305–321.
[4] J.G. Williams, P.D. Ewing, Fracture under complex stress—the angled crack problem, Int. J. Fract. 8 (4) (1972) 416–441.
[5] Y. Ueda, K. Ikeda, T. Yao, M. Aoki, Characteristics of brittle failure under general combined modes including those under bi-axial tensile loads, Engrg. Fract. Mech. 18 (6) (1983) 1131–1158.
[6] M.L. Williams, On the stress distribution at the base of a stationary crack, J. Appl. Mech., Trans. ASME 24 (1) (1957) 109–114.
[7] Y.-J. Chao, X.H. Zhang, Constraint effect in brittle fracture, in: R.S. Piascik, J.C. Newman, D.E. Dowling (Eds.), Fatigue and Fracture Mechanics, ASTM STP1296, American Society for Testing and Materials, Philadelphia, PA, 1997, pp. 41–60.
[8] D. Richardson, J.G. Goree, Experimental varification of a new two-parameter fracture model, in: R. Chona (Ed.), Fracture Mechanics: Twenty-third Symposium ASTM STP 1189, American Society for Testing and Materials, Philadelphia, PA, 1993, pp. 738–751.
[9] J. Eftis, N. Subramonian, H. Liebowitz, Crack border stress and displacement equations revisited, Engrg. Fract. Mech. 9 (1) (1977) 189–210.
[10] J.W. Eischen, Fracture of non-homogeneous materials, Int. J. Fract. 34 (1) (1987) 3–22.
[11] J.-H. Kim, G.H. Paulino, Finite element evaluation of mixed-mode stress intensity factors in functionally graded materials, Int. J. Numer. Meth. Engrg. 53 (8) (2002) 1903–1935.
[12] P.R. Marur, H.V. Tippur, Numerical analysis of crack-tip fields in functionally graded materials with a crack normal to the elastic gradient, Int. J. Solids Struct. 37 (38) (2000) 5353–5370.
[13] J.F. Yau, S.S. Wang, H.T. Corten, A mixed-mode crack analysis of isotropic solids using conservation laws of elasticity, J. Appl. Mech. Trans. ASME 47 (2) (1980) 335–341.
[14] S.S. Wang, H.T. Corten, J.F. Yau, Mixed-mode crack analysis of rectilinear anisotropic solids using conservation laws of elasticity, Int. J. Fract. 16 (3) (1980) 247–259.
[15] J.F. Yau, Mixed-mode fracture analysis using a conservation integral, Ph.D. Thesis, Department of Theoretical and Applied Mechanics, University of Illinois at Urbana-Champaign, 1979.
[16] J. Dolbow, M. Gosz, On the computation of mixed-mode stress intensity factors in functionally graded materials, Int. J. Solids Struct. 39 (9) (2002) 2557–2574.
[17] B.N. Rao, S. Rahman, Mesh-free analysis of cracks in isotropic functionally graded materials, Engrg. Fract. Mech. 70 (1) (2003) 1–27.
[18] J.-H. Kim, G.H. Paulino, An accurate scheme for mixed-mode fracture analysis of functionally graded materials using the interaction integral and micromechanics models, Int. J. Numer. Meth. Engrg., in press.
[19] D.J. Smith, M.R. Ayatollahi, M.J. Pavier, The role of T-stress in brittle fracture for linear elastic materials under mixed-mode loading, Fatigue Fract. Engrg. Mater. Struct. 24 (2) (2001) 137–150.
[20] B. Cotterell, J.R. Rice, Slightly curved or kinked cracks, Int. J. Fract. 16 (2) (1980) 155–169.
[21] Z.-Z. Du, J.W. Hancock, The effect of non-singular stresses on crack-tip constraint, J. Mech. Phys. Solids 39 (3) (1991) 555–567.
[22] N.P. O'Dowd, C.F. Shih, R.H. Dodds Jr., The role of geometry and crack growth on constraint and implications for ductile/brittle fracture, in: Constraint Effects in Fracture Theory and Applications, vol. 2 of ASTM STP 1244, American Society for Testing and Materials, 1995, pp. 134–159.
[23] S.G. Larsson, A.J. Carlson, Influence of non-singular stress terms and specimen geometry on small-scale yielding at crack tips in elastic–plastic materials, J. Mech. Phys. Solids 21 (4) (1973) 263–277.
[24] P.S. Leevers, J.C.D. Radon, Inherent stress biaxiality in various fracture specimen, Int. J. Fract. 19 (4) (1982) 311–325.
[25] G.E. Cardew, M.R. Goldthorpe, I.C. Howard, A.P. Kfouri, On the elastic T-term, Fundamentals of Deformation and Fracture: Eshelby Memorial Symposium, 1985.
[26] A.P. Kfouri, Some evaluations of the elastic T-term using Eshelby's method, Int. J. Fract. 30 (4) (1986) 301–315.
[27] J. Sladek, V. Sladek, P. Fedelinski, Contour integrals for mixed-mode crack analysis: effect of nonsingular terms, Theor. Appl. Fract. Mech. 27 (2) (1997) 115–127.
[28] C.S. Chen, R. Krause, R.G. Pettit, L. Banks-Sills, A.R. Ingraffea, Numerical assessment of T-stress computation using a *p*-version finite element method, Int. J. Fract. 107 (2) (2001) 177–199.
[29] E.M. Carrillo-Heian, R.D. Carpenter, G.H. Paulino, J.C. Gibeling, Z.A. Munir, Dense layered molybdenum disilicide-silicon carbide functionally graded composites formed by field-activated synthesis, J. Am. Ceramic Soc. 84 (5) (2001) 962–968.
[30] Z.-H. Jin, G.H. Paulino, Transient thermal stress analysis of an edge crack in a functionally graded material, Int. J. Fract. 107 (1) (2001) 73–98.
[31] T.L. Anderson, Fracture Mechanics: Fundamentals and Applications, CRC Press LLC, Boca Raton, 1995.
[32] T.L. Becker Jr., R.M. Cannon, R.O. Ritchie, Finite crack kinking and T-stresses in functionally graded materials, Int. J. Solids Struct. 38 (32–33) (2001) 5545–5563.
[33] G.H. Paulino, J.-H. Kim, A new approach to compute T-stress in functionally graded materials using the interaction integral method, in preparation.
[34] Z.-H. Jin, N. Noda, Crack-tip singular fields in nonhomogeneous materials, J. Appl. Mech., Trans. ASME 61 (3) (1994) 738–740.
[35] S.P. Timoshenko, J.N. Goodier, Theory of Elasticity, third ed., McGraw-Hill, New York, 1987.

[36] J.R. Rice, A path-independent integral and the approximate analysis of strain concentration by notches and cracks, J. Appl. Mech., Trans. ASME 35 (2) (1968) 379–386.
[37] I.S. Raju, K.N. Shivakumar, An equivalent domain integral method in the two-dimensional analysis of mixed mode crack problems, Engrg. Fract. Mech. 37 (4) (1990) 707–725.
[38] R.D. Cook, D.S. Malkus, M.E. Plesha, Concepts and applications of finite element analysis, third ed., John Wiley & Sons Inc., New York, 1989.
[39] S. Nemat-Nasser, Micromechanics: Overall Properties of Heterogeneous Materials, North-Holland, The Netherlands, 1993.
[40] A.L. Kalamkarov, A.G. Kolpakov, Analysis, design and optimization of composite structures, John Wiley & Sons, Chichester, 1997.
[41] J. Aboudi, M.J. Pindera, S.M. Arnold, Higher-order theory for functionally graded materials, Compos. Part B—Engrg. 30 (8) (1999) 777–832.
[42] J. Aboudi, M.J. Pindera, S.M. Arnold, Microstructural optimization of functionally graded composites subjected to a thermal gradient via the coupled higher-order theory, Compos. Part B—Engrg. 28 (1-2) (1997) 93–108.
[43] G.J. Zuiker, G.J. Dvorak, The effective properties of functionally graded composites—I, Extension of the Mori–Tanaka method to linearly varying fields, Compos. Engrg. 4 (1) (1994) 19–35.
[44] T. Reiter, G.J. Dvorak, V. Tvergaard, Micromechanical models for graded composite materials, J. Mech. Phys. Solids 45 (8) (1997) 1281–1302.
[45] T. Reiter, G.J. Dvorak, Micromechanical models for graded composite materials: II, thermomechanical loading, J. Mech. Phys. Solids 46 (9) (1998) 1655–1673.
[46] A.V. Hershey, The elasticity of an isotropic aggregate of anisotropic cubic crystals, J. Appl. Mech., Trans. ASME 21 (2) (1954) 236–240.
[47] B. Budiansky, On the elastic moduli of some heterogeneous materials, J. Mech. Phys. Solids 13 (4) (1965) 223–227.
[48] R. Hill, Continuum micro-mechanics of elastic–plastic polycrystals, J. Mech. Phys. Solids 13 (2) (1965) 89–101.
[49] R. Hill, A self-consistent mechanics of composite materials, J. Mech. Phys. Solids 13 (4) (1965) 213–222.
[50] T. Mori, K. Tanaka, Average stress in matrix and average elastic energy of materials with misfitting inclusions, Acta Mater. 21 (5) (1973) 571–574.
[51] Z. Hashin, S. Shtrikman, A variational approach to the theory of the elastic behavior of multiphase materials, J. Mech. Phys. Solids 11 (2) (1963) 127–140.
[52] P.A. Wawrzynek, Interactive finite element analysis of fracture processes: an integrated approach, M.S. Thesis, Cornell University, 1987.
[53] P.A. Wawrzynek, A.R. Ingraffea, Discrete modeling of crack propagation: theoretical aspects and implementation issues in two and three dimensions, Report 91-5, School of Civil Engineering and Environmental Engineering, Cornell University, 1991.
[54] J.-H. Kim, G.H. Paulino, Isoparametric graded finite elements for nonhomogeneous isotropic and orthotropic materials, J. Appl. Mech., Trans. ASME 69 (4) (2002) 502–514.
[55] G.H. Paulino, J.-H. Kim, The weak patch test for nonhomogeneous materials modeled with graded finite elements, in preparation.
[56] G.H. Paulino, Z. Dong, A novel application of the singular integral equation approach to evaluate T-stress in functionally graded materials, in preparation.
[57] R.D. Carpenter, W.W. Liang, G.H. Paulino, J.C. Gibeling, Z.A. Munir, Fracture testing and analysis of a layered functionally graded Ti/TiB beam in 3-point bending, Mater. Sci. Forum 308–311 (1999) 837–842.
[58] Z.-H. Jin, G.H. Paulino, R.H. Dodds Jr., Finite element investigation of quasi-static crack growth in functionally graded materials using a novel cohesive zone fracture model, J. Appl. Mech., Trans. ASME 69 (3) (2002) 370–379.
[59] J.M. Ambrico, E.E. Jones, M.R. Begley, Cracking in thin multi-layers with finite width and periodic architectures, Int. J. Solids Struct. 39 (6) (2002) 1443–1462.